
RIT Munsell Color Science Laboratory

Research and Development Final Report

**The Spectral Modeling of
Large-Format Ink-Jet Printers**

Submitted to:
**Hewlett Packard
Barcelona Division**

Submitted by:
**Roy S. Berns
Animesh Bose
Di-Yuan Tzeng**
Munsell Color Science Laboratory
Chester F. Carlson Center for Imaging Science
Rochester Institute of Technology
54 Lomb Memorial Drive
Rochester, New York 14623-5604 USA
(716) 475-2230
Fax: (716) 475-5988
Internet: rsbpph@rit.edu

December 1996

Executive Summary

A one-year research and development program was undertaken to colorimetrically characterize large-format ink-jet printers manufactured by Hewlett Packard. Most of the research was performed using the HP650C. Near the end of the project, an HP755CM was used to exemplify the techniques developed on the HP650C. Prints were produced using the "scatter" mode halftoning algorithm on to uncoated ink-jet paper.

It was hypothesized that spectral-based models would provide equivalent characterization accuracy in comparison to direct table look up methods based on exhaustive measurements. Model-based approaches have the advantages of faster recharacterization and the opportunity of simulating product enhancements such as changes in ink properties and halftoning. The Murray-Davies, Yule-Nielsen-Murray-Davies, and transparent-Kubelka-Munk-continuous-tone models were used for spectral reconstruction. The Yule-Nielsen-Murray-Davies model resulted in the best spectral reconstruction accuracy followed by the Kubelka-Munk model.

Because the "scatter" mode halftoning algorithm is based on the same FM screening for each color plane, this yields the same number of color types as cluster-dot halftoning (also referred to as dot-on-dot or non-rotated screen printing). Thus, the usual cluster-dot halftone algorithm was used convert from digital code values to the particular colors that would appear in a halftone cell. Unfortunately, the results were unsatisfactory. Upon magnification, the four color planes were not in perfect registration resulting in more color types than expected. This led to devising a relaxed-cluster-dot halftone algorithm (similar to Neugebauer) to convert from digital code values to color types. This algorithm in conjunction with the Yule-Nielsen-Murray-Davies model has the potential of predicting 729 colors sampling the printer's color gamut to an average accuracy of $1.2 \Delta E_{ab}^*$. However, because the relaxed-cluster-dot algorithm was not a true representation of the digital to ink conversion, a result of a complex and proprietary conversion pipeline, it was impossible to use the model in building an acceptable device profile for use in color management. Since this pipeline is readily available to Hewlett Packard, the modeling approach used in this research can be applied easily to building device profiles and product development. This report details techniques to modeling the spectral properties of large-format inkjet printers manufactured by Hewlett Packard. The principles described herein can be applied to any color imaging process.

Table of Contents

I.	Background on Modeling the Color Properties of Imaging Devices	1
II.	Methods for Model Evaluation.....	7
III.	Experimental Example Using HP755CM Large Format Printer.....	25
	Dataset.....	25
	Assumed Halftoning Algorithm.....	27
	Model Evaluation: Murray-Davies Equation.....	30
	Model Evaluation: Yule-Nielsen-Murray-Davies Equation.....	33
	Model Evaluation: Yule-Nielsen-Murray-Davies Equation With Relaxed Colorant Selector	38
	Model Evaluation: Continuous Tone Using Kubelka-Munk Equation	43
	Selecting the Optimal Model.....	46
IV.	Summary and Conclusions.....	51
V.	General References.....	52

I. Background on Modeling the Color Properties of Imaging Devices

The color modeling of imaging devices, that is, describing the relationship between digital and spectral or colorimetric data, can be thought of as a two-stage process. The first stage consists of “finding the linear model.” Essentially, the goal is to find a linear or nonlinear transformation of color-measurement data (*e.g.*, spectral reflectance factor, spectral transmittance, spectral radiance, tristimulus values) where the colorants and their mixtures can be described using linear algebra. The second stage defines the relationship between “user controls” and the scalars associated with the linear description of each colorant. A computer-controlled CRT display exemplifies this approach.

The “business” end of a CRT is the excitation and emission of three colored phosphors. We can measure the emitted light using a spectroradiometer, for example, as shown in Fig. 1 for five excitation/emission levels of each channel. The first step is identifying and verifying the transformation of the fundamental measurement yielding a linear system. In the specific case of displays, the spectral radiance is the linear system. We can test this graphically by normalizing each measurement by its peak output:

$$L_{\lambda,\text{normalized}} = \frac{L_{\lambda,\text{measured}}}{L \text{ at } \lambda \text{ maximum}} \quad (1)$$

where L_{λ} is spectral radiance. The data plotted in Fig. 1 would result in three distinct curves, one for each channel. Any deviation from this scaleability would be due to measurement noise or model limitations. This implies that from a single measurement of each channel (“colorant”) at its peak output, we can predict all of the other measurements if we know how much to scale the peak values, denoted by R, G, and B and shown in Eq. (2) for the red channel.

$$L_{\lambda,r} = RL_{\lambda,r,\text{max}} \quad (2)$$

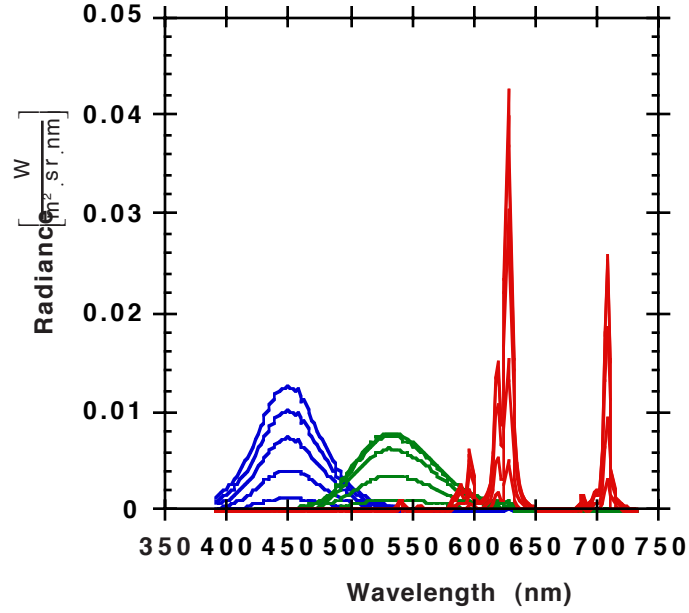


Fig. 1. Spectral radiance measurement of red, green, and blue channels and five levels of excitation.

The second aspect of describing the system using linear algebra is the additivity of each channel, the “color mixing of each colorant.” At viewing distances and refresh rates typical of computer-controlled CRT displays, the spectral radiance of a pixel is the linear combination of the spectral radiances of the three channels:

$$L_{\lambda, \text{pixel}} = RL_{\lambda, r, \text{max}} + GL_{\lambda, g, \text{max}} + BL_{\lambda, b, \text{max}} \quad (3)$$

Thus, the first stage of modeling a computer-controlled CRT display* is described by Eq. (4) using matrix notation:

*This is a theoretical description assuming channel independence and suitable accounting of ambient and internal flare.

$$\begin{bmatrix} L_{\lambda=1} \\ \cdot \\ \cdot \\ \cdot \\ L_{\lambda=n} \end{bmatrix}_{\text{pixel}} = \begin{bmatrix} L_{\lambda=1,r,\text{max}} & L_{\lambda=1,g,\text{max}} & L_{\lambda=1,b,\text{max}} \\ \cdot & \cdot & \cdot \\ \cdot & \cdot & \cdot \\ \cdot & \cdot & \cdot \\ L_{\lambda=n,r,\text{max}} & L_{\lambda=n,g,\text{max}} & L_{\lambda=n,b,\text{max}} \end{bmatrix} \begin{bmatrix} R \\ G \\ B \end{bmatrix} \quad (4)$$

Since the spectral radiances are additive, we can rewrite Eq. (4) in terms of tristimulus values:

$$\begin{bmatrix} X \\ Y \\ Z \end{bmatrix}_{\text{pixel}} = \begin{bmatrix} X_{r,\text{max}} & X_{g,\text{max}} & X_{b,\text{max}} \\ Y_{r,\text{max}} & Y_{g,\text{max}} & Y_{b,\text{max}} \\ Z_{r,\text{max}} & Z_{g,\text{max}} & Z_{b,\text{max}} \end{bmatrix} \begin{bmatrix} R \\ G \\ B \end{bmatrix} \quad (5)$$

From Eq. 2, R, G, and B are radiometric scalars. From a colorimetrist's point of view, they are also tristimulus values. Accordingly, any radiometric ratio can be used to measure, R, G, or B. Eq. (6) provides two examples:

$$\begin{aligned} R &= \frac{Y}{Y_{\text{max}}} \\ R &= \frac{\int_{\lambda} L_{\lambda} d\lambda}{\int_{\lambda} L_{\lambda_{\text{peak}}} d\lambda} \end{aligned} \quad (6)$$

The second stage is relating the "user controls" with the linear-equation scalars. In the case of computer-controlled CRT displays, the user controls refer to digital data defining an image. Eq. (7) is often used to relate the well-known nonlinearity between digital and radiometric data.

$$R = \left(k_{g,r} \left(\frac{d_r}{2^N - 1} \right) + k_{o,r} \right)^{y_r} \quad (7)$$

where N counts the number of bits in the digital-to-analog converter, k_g is a system gain term, k_o is a system offset term, and γ is an exponent. This nonlinearity is shown in Fig. 2.

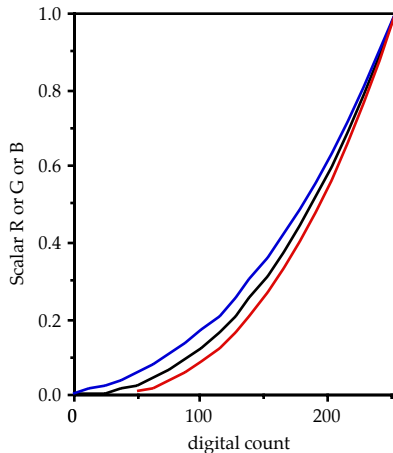


Fig. 2. Typical nonlinear relationship between digital and radiometric data for a computer-controlled CRT display.

The CRT model is a nonlinear stage described by three functions or one-dimensional look-up tables followed by a three-by-three linear matrix. (This modeling definition lends itself well to building device profiles using ICC protocols.)

Turning to ink-jet printers, the first step is to find the linear system. Theoretically, a given color is a summation of the spectral reflectance factors, R_{λ} , of each of the pixels comprising the halftone cell. This is described by Eq. (8):

$$R_{\lambda} = \sum_i R_{\lambda,i} \quad (8)$$

where i counts the number of unique color types. The number of color types depends on the halftoning algorithm. In the case of the HP650C and HP755CM, the “scatter mode” is a FM-based algorithm where each color plane has the identical FM screening. This is equivalent to non-rotated screening in conventional printing. Assuming perfect registration, overprints of each primary result in a single color type. For example, magenta and yellow, each at 50% area coverage, will result in

only red pixels. Their area coverage, in theory, will be 50%. The key issue is the number of color types, not their spatial distribution within a halftone cell or across a larger image area. This is shown in Fig. 3 for a light-red color. For the ink-jet halftoning (or non-rotated screening), one would only see red dots on the page. If the screens were at different effective angles for each color plane, there would be three color types, magenta, yellow, and their overprint, red. The non-rotated color formation is often called “cluster dot” or “dot on dot” while the rotated color formation is often referred to as “Neugebauer.”



Fig. 3. Halftone representation of continuous-tone color (left) using non-rotated (middle) and conventional rotated (right) screening. (Photoshop stylize plug in used to generate images.)

Predicting the spectral reflectance factor, and hence the color, would require different equations depending on the number of color types. Based on the above example, one needs to measure the spectral reflectance factor of the paper and the 100% area coverage of the red secondary for cluster-type algorithms. For Neugebauer-type algorithms, one also needs the spectral data of the individual primaries.

Many ink-jet printers use the maximum amount of black possible in their transformation from red, green, and blue digital code values to the amounts of cyan, magenta, yellow, and black ink applied to the substrate. This has the advantage of reducing the cost per page, increasing printing speed, and increasing the effective resolution of images since black ink tends to exhibit lower dot gain. From our evaluations of the HP650C and HP755CM printers, this approach seems to have been taken.

Thus the conversion between digital data and the area coverage of each color type, in theory, is shown by Eqs. (9) and (10) for cluster-dot printing with maximum ink where Eq. (9) generates the amount of black and Eq. (10) determines the amount of each color type observable on the substrate. The cluster-dot algorithm results in black, one primary, and one secondary color type within any halftone cell.

$$\begin{aligned}
d_k &= \min(255 - d_r, 255 - d_g, 255 - d_b) \\
d_c &= 255 - d_r - d_k \\
d_m &= 255 - d_g - d_k \\
d_y &= 255 - d_b - d_k.
\end{aligned} \tag{9}$$

$$\begin{aligned}
a_r &= \min(d_m, d_y) / 255 \\
a_g &= \min(d_c, d_y) / 255 \\
a_b &= \min(d_c, d_m) / 255 \\
a_c &= (d_c / 255) - a_g - a_b \\
a_m &= (d_m / 255) - a_r - a_b \\
a_y &= (d_y / 255) - a_r - a_g \\
a_k &= (d_k / 255) \\
a_w &= 1 - a_r - a_g - a_b - a_c - a_m - a_y - a_k
\end{aligned} \tag{10}$$

Once the area coverages are calculated, one can predict spectral reflectance factor using Eq. (11) or tristimulus values using Eq. (12).

$$R_\lambda = a_k R_{\lambda,k} + a_p R_{\lambda,p} + a_s R_{\lambda,s} + a_w R_{\lambda,w} \tag{11}$$

$$\begin{aligned}
X &= a_k X_k + a_p X_p + a_s X_s + a_w X_w \\
Y &= a_k Y_k + a_p Y_p + a_s Y_s + a_w Y_w \\
Z &= a_k Z_k + a_p Z_p + a_s Z_s + a_w Z_w
\end{aligned} \tag{12}$$

The above printer model assumes a linear relationship between the “user controls” (digital code values) and the area coverages of each color type. In practice, dots spread in their area coverage. This is known as mechanical dot gain and is an

integral component of the color modeling of ink-jet printing (or any type of printing, for that matter). This introduces a nonlinear stage to the model, similar to the nonlinear stage of CRT imaging. As an example, the dot-gain function required to model this nonlinear stage for a typical desktop ink-jet printer is shown in Fig. 4. Thus, between Eqs. (10) and either (11) or (12), nonlinear equations or one-dimensional look-up tables are required.

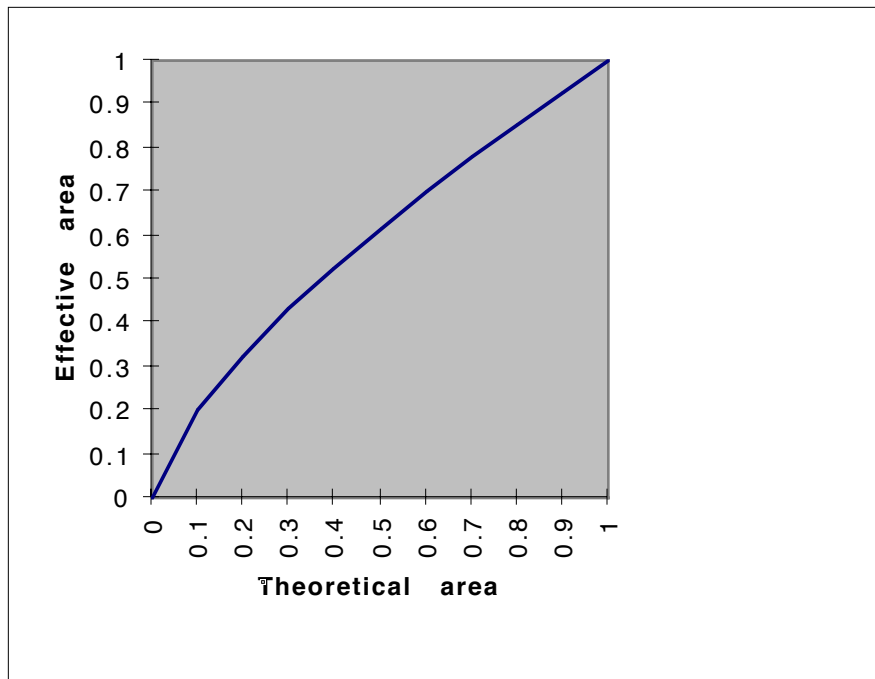


Fig. 4. Typical mechanical dot gain for a desktop ink-jet printer.

For the HP650C or HP755CM, the theoretical model consists of color-type selection, nonlinear mechanical dot gain, and additivity of the spectral reflectance factors (or tristimulus values) of each color type within the halftone cell. The last two steps are similar conceptually to modeling computer-controlled CRT displays.

II. Methods for Model Evaluation

The key model component requiring verification is the linear model stage. Can primary ramps be estimated from a single measurement? Can mixtures be predicted? Recall the theoretical equation for ink-jet printers given above: Is Eq. (11) correct?

The first step is to evaluate each primary ramp. Samples are made with various amounts of ink on paper, such as shown in Fig. 5.

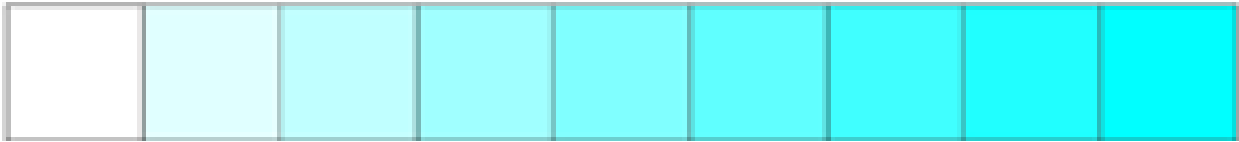


Fig. 5. Primary ramp.

The spectral reflectance factors are measured using a spectrophotometer, as shown in Fig. 6 where c0 represents the paper and c100 represents 100% area coverage of the cyan ink.

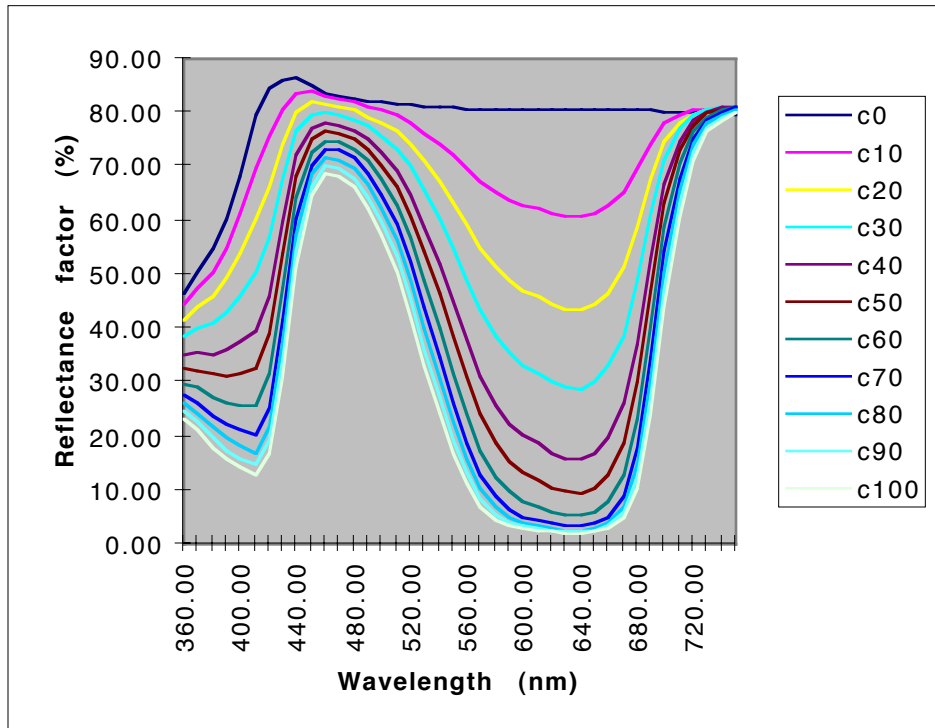


Fig. 6. Measured spectral reflectance factor data of cyan ramp printed using HP650C.

Theoretically, Eq. (13), the Murray-Davies equation, should model each color based on the maximum amount of ink on paper and the paper substrate:

$$R_{\lambda} = a_c R_{\lambda,c} + (1 - a_c) R_{\lambda,w} \quad (13)$$

Since the mechanical dot gain is, as yet, unknown, regression analysis is used to evaluate model accuracy. Eq. (13) can be rewritten as a linear equation, appropriate for linear regression:

$$(R_{\lambda} - R_{\lambda,w}) = a_c (R_{\lambda,c} - R_{\lambda,w}) \quad (14)$$

Using regression-analysis terminology, this is equivalent to Eq. (15):

$$\mathbf{Y} = \beta \mathbf{X} \quad (15)$$

where

$$\begin{aligned} \mathbf{Y} &= (R_{\lambda} - R_{\lambda,w}) \\ \mathbf{X} &= (R_{\lambda,c} - R_{\lambda,w}) \\ \beta &= a_c \end{aligned} \quad (16)$$

Through least squares, Eq. (17), the fractional area, a_c , is estimated.

$$\mathbf{b} = (\mathbf{X}^T \mathbf{X})^{-1} \mathbf{X}^T \mathbf{Y} \quad (17)$$

For example, the 50% cyan sample was predicted using Systat, a statistics software package. The Systat dialog box is shown in Fig. 7 and the model prediction in Fig. 8.

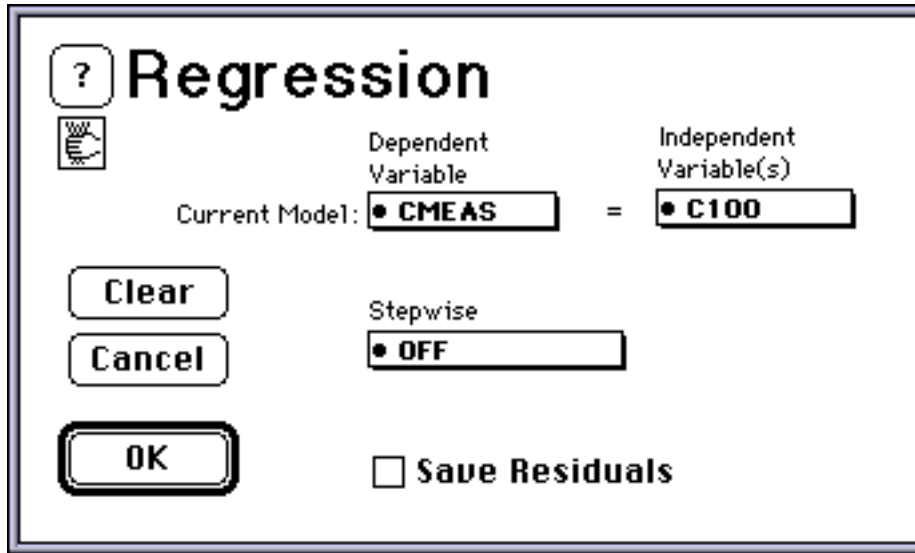


Fig. 7. Dialog box for Systat's regression procedure.

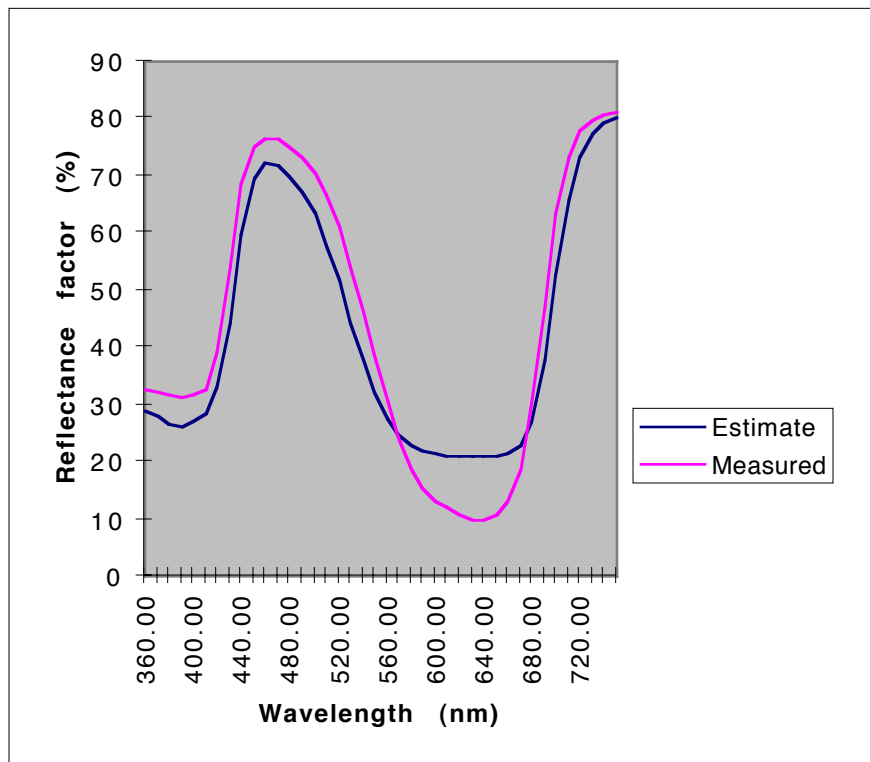


Fig. 8. Linear model prediction for 50% cyan using Eq. (14).

The prediction shown in Fig. 8 is typical of spectral regression results for models with low accuracy. Because of the least-squares matching criterion, the estimated spectral reflectance factor is both under- and over-predicted about the

measured curve. This model prediction accuracy is representative of all of the ramp samples. This suggests that the theoretical model does not adequately predict the spectral properties of this printer, necessitating a model modification or new model.

A second method to quantify model appropriateness is to perform an eigenvector analysis on the primary-ramp data. If Eq. (14) is correct, the first eigenvector of the ramp measurements (with the paper subtracted) should account for a very high percentage of the total reflectance factor variance. The transposed reflectance factor data (each column represents a wavelength) are analyzed using principal component analysis. The dialog box is shown in Fig. 9. Linear models with excellent fit should result in their first eigenvector accounting for greater than 99.9% of the total variance. For these data, the first eigenvector only accounted for 97.73% of the total variance.

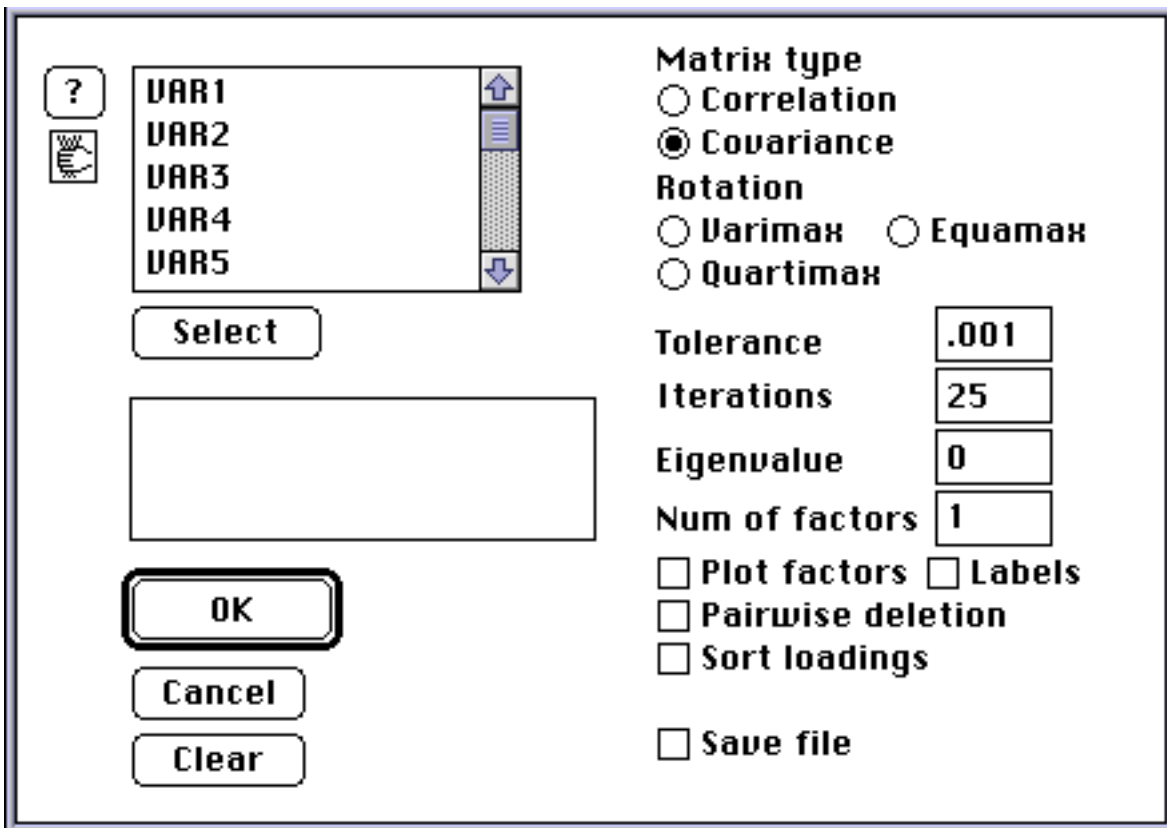


Fig. 9. Dialog box for Systat's principal component analysis procedure.

The low model accuracy can be shown graphically by plotting normalized spectra according to Eq. (18). This is shown in Fig 10 where 630 nm was selected as

the minimum reflectance factor (corresponding to the peak absorption). For correct models, the spectra should overlay one another. Clearly, the Murray-Davies equation is not modeling the color formation of the HP650C.

$$R_{\lambda, \text{normalized}} = \frac{R_{\lambda, c} - R_{\lambda, w}}{(R_c - R_w) \text{ at } \lambda \text{ minimum}} \quad (18)$$

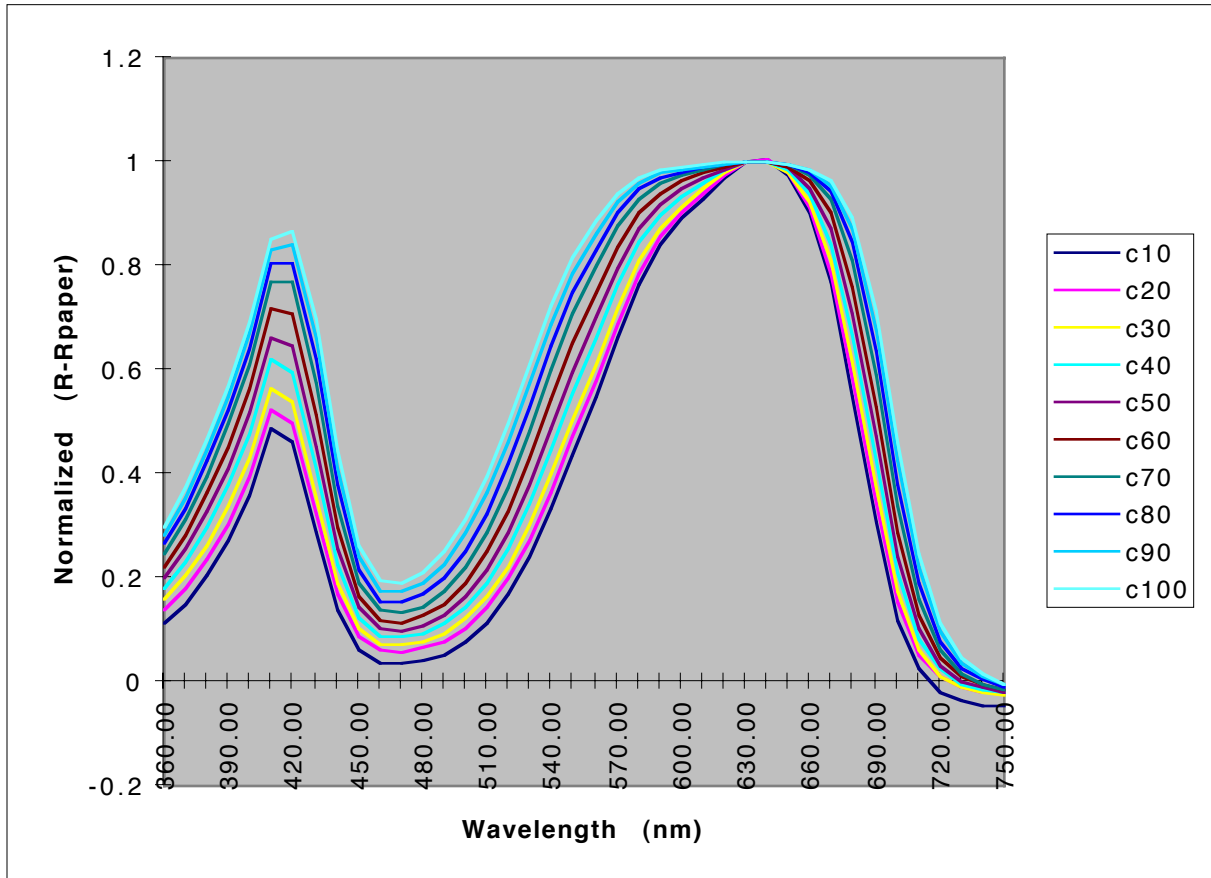


Fig. 10. Normalized reflectance factor spectra for cyan ramp data.

Thus, the first step for model effectiveness indicated that the theoretical model was inappropriate. Often, the Murray-Davies equation is modified by the Yule-Nielsen n-value correction, given by Eq. (19). Theoretical justifications for the use of n were first described by Yule and Nielsen and relate to light scattering within the paper. Simply, because of the paper spread function, there are paper-ink optical interactions resulting in spectra that behave distinct from the ink at 100% area

coverage. When n is an integer value, this defines the number of distinct ink types (from an optical perspective).

$$R_\lambda = \left(a_c R_{\lambda,c}^{1/n} + (1 - a_c) R_{\lambda,w}^{1/n} \right)^n \quad (19)$$

It has been suggested by Pearson that an n of 1.7 is reasonable for offset printing. The normalized spectra are shown in Fig. 11 using $n=1.7$. Although the curves are not identical, there is clear improvement in comparison to Fig. 10.

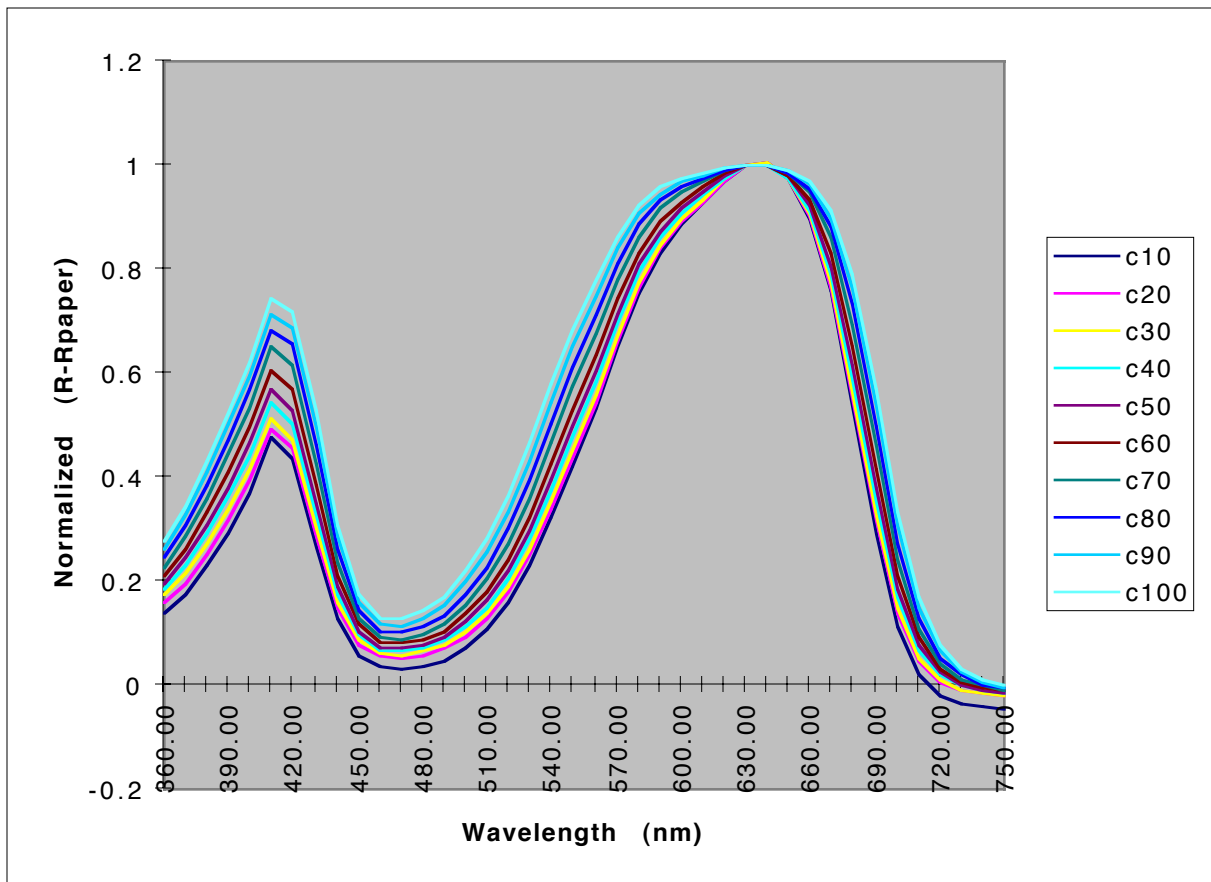


Fig. 11. Normalized reflectance factor spectra for cyan-ramp data with $n=1.7$.

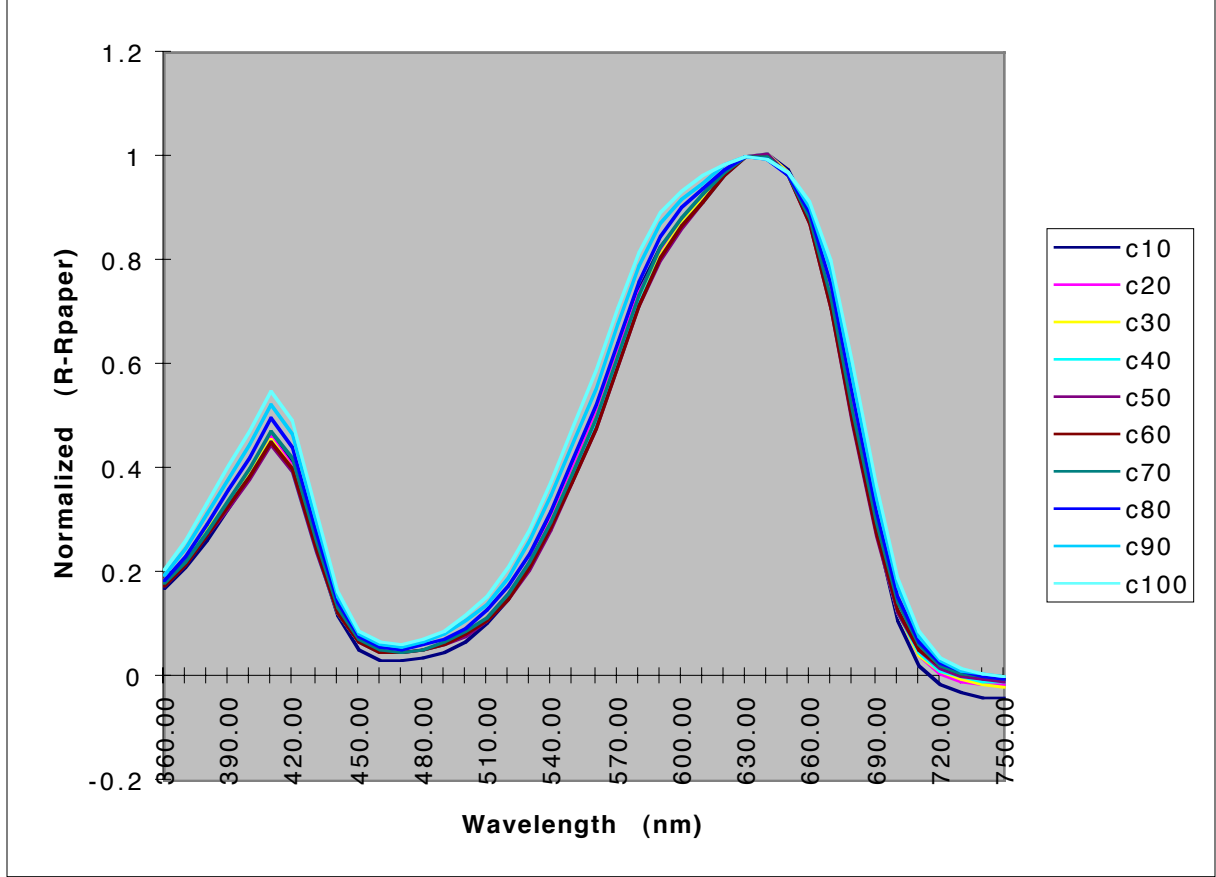


Fig. 12. Normalized reflectance factor spectra for cyan-ramp data with $n=10$.

Note that as n increases, one moves from halftone to continuous tone. Figure 12 is a plot of normalized reflectance factor spectra for $n=10$. This yields the most similar spectra. This led to the model described in previous progress reports, the Kubelka-Munk transparent model given in Eq. (20). The assumption that led to its use was that the combination of FM screening and high resolution yielded color mixing equivalent to premixing the inks in a single pen and applying the ink at different concentrations to yield modulated color, i.e., continuous tone.

$$R_{\lambda, \text{measured}} = R_{\lambda, \text{paper}} \exp\left\{-2\left(c_{\text{cyan}} k_{\lambda, \text{cyan}} + c_{\text{magenta}} k_{\lambda, \text{magenta}} + c_{\text{yellow}} k_{\lambda, \text{yellow}}\right)\right\} \quad (20)$$

where c represents concentration and k_{λ} defines the absorptivity of each color type. (The determination of k_{λ} will be described below.)

A linear model can be used to predict primary-ramp colors using Eq. (21) to define the regression model parameters.

$$\begin{aligned}
 \mathbf{Y} &= -0.5 \ln \left\{ R_{\lambda, \text{measured}} / R_{\lambda, \text{paper}} \right\} \\
 \mathbf{X} &= \left(k_{\lambda, \text{cyan}} \right) \\
 \beta &= c_{\text{cyan}}
 \end{aligned}
 \tag{21}$$

Using Eqs. (21) and (17), the 50% cyan sample was predicted again using measured data of the 100% cyan sample and the paper substrate. The prediction is shown in Fig. 13. Comparing this prediction with that using the spectral reflectance factor data shows the significant improvement in model-prediction accuracy.

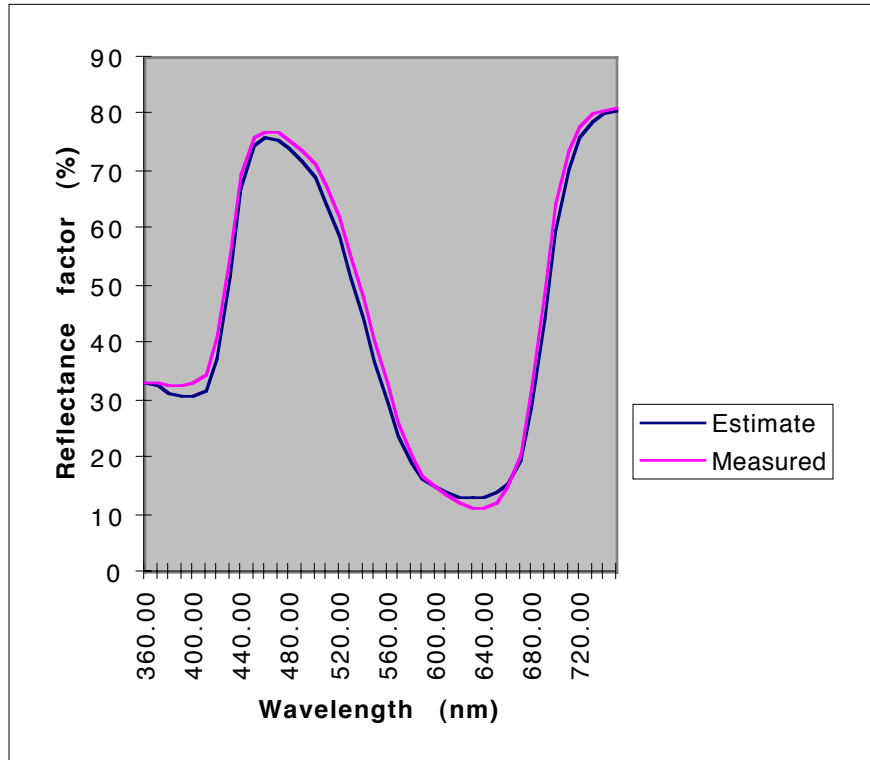


Fig. 13. Linear model prediction for 50% cyan using Eqs. (17) and (21).

An eigenvector analysis on all the ramp data expressed in absorption (K) units resulted in a first eigenvector with a 99.686% total variance accountability.

The normalized spectra based on absorption data are shown in Fig. 14; the reasonable spectral similarity supports the use of Kubelka-Munk theory.

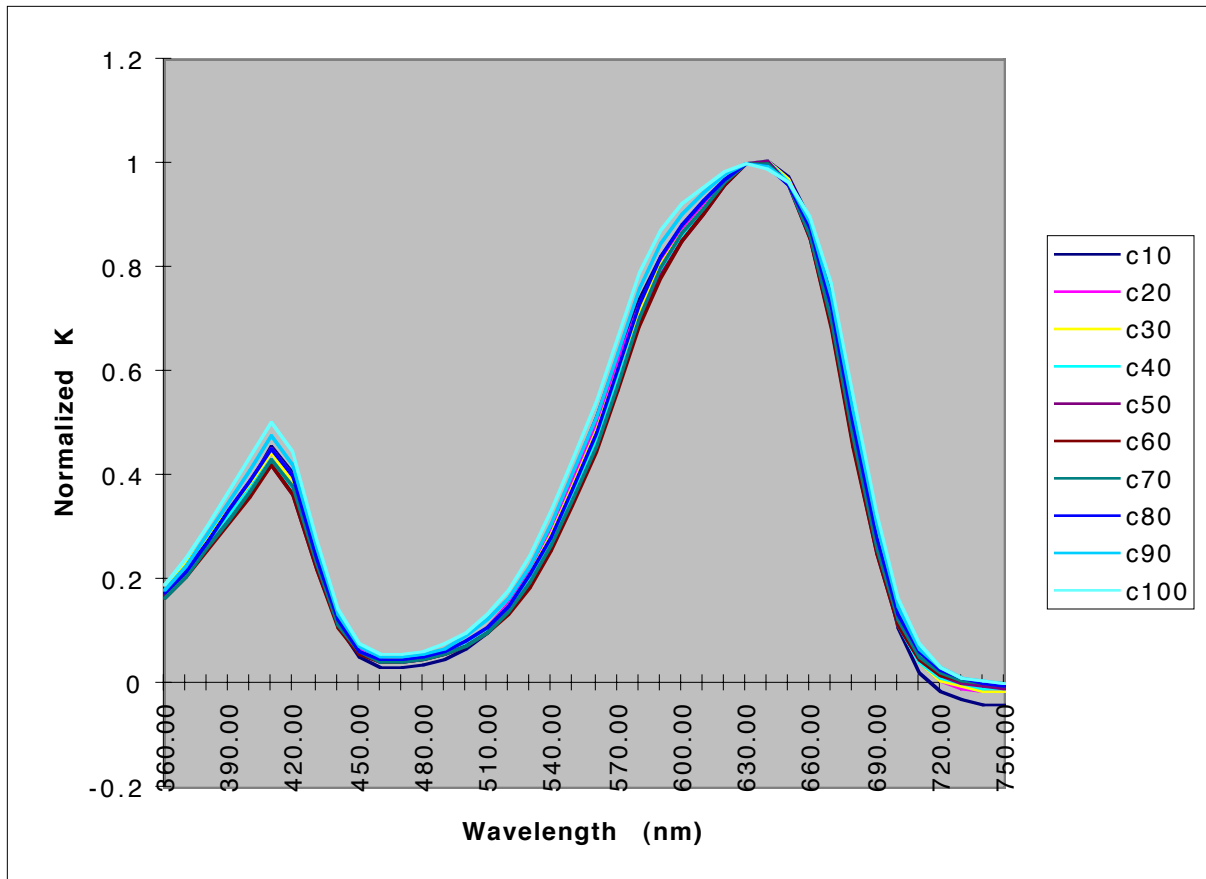


Fig. 14. Normalized absorption spectra for cyan-ramp data.

Goodness can be evaluated several ways. The obvious method is to calculate RMS spectral error. It is also important to calculate colorimetric goodness metrics. The usual method is to calculate CIELAB total color differences, ΔE^*_{ab} . This is shown below in Table I for the cyan-ramp samples estimated using Eq. (18) with a RMS spectral error minimization criterion.

Table I. Colorimetric accuracy for spectral matching using Eq. (20) for cyan-ramp.

	c_{cyan}	$\Delta E_{\text{ab}}^* \text{ D50}$	$\Delta E_{\text{ab}}^* \text{ ill A}$
c0	0.01	0.49	0.55
c10	0.23	0.38	0.36
c20	0.49	0.30	0.29
c30	0.79	0.28	0.41
c40	1.22	1.30	1.63
c50	1.56	2.35	2.91
c60	1.96	3.06	3.84
c70	2.33	2.70	3.37
c80	2.59	1.31	1.65
c90	2.83	0.55	0.65
c100	3.04	2.20	2.72

Because colorimetric accuracy is more important than spectral accuracy (particularly when building device profiles), we can use a tristimulus matching algorithm rather than a spectral matching algorithm. Nonlinear optimization is useful where ΔE_{ab}^* between measured and estimated spectra are minimized. This is shown in Table II. (However, care must be taken here. Colorimetric algorithms have three degrees of freedom; colors to be matched should have three inks in their composition. As shown in Table II, the other colorants have slight negative values.) Using two illuminants that are very spectrally dissimilar is an effective method to judge spectral fit. If the secondary illuminant results in large color differences, the model, likely, is suboptimal.

Table II. Colorimetric accuracy for tristimulus matching using Eq. 20.

	c_{cyan}	c_{magenta}	c_{yellow}	$\Delta E_{\text{ab}}^* \text{ D50}$	$\Delta E_{\text{ab}}^* \text{ ill A}$
c0	0.01	0.01	0.01	0.00	0.06
c10	0.23	0.01	0.00	0.00	0.04
c20	0.48	0.00	0.00	0.00	0.09
c30	0.79	0.00	0.00	0.00	0.16
c40	1.24	-0.02	0.00	0.00	0.29
c50	1.61	-0.04	0.00	0.00	0.42
c60	2.04	-0.06	-0.01	0.00	0.53
c70	2.42	-0.06	-0.01	0.00	0.42
c80	2.64	-0.03	0.00	0.00	0.22
c90	2.81	0.01	0.00	0.00	0.03
c100	2.95	0.06	0.01	0.00	0.32

Following the model selection based on primary-ramp analyses, the next step is to predict mixtures based on Eq. (22):

$$R_{\lambda, \text{measured}} = R_{\lambda, \text{paper}} \exp\left\{-2\left(c_{\text{primary}}k_{\lambda, \text{primary}} + c_{\text{secondary}}k_{\lambda, \text{secondary}} + c_{\text{black}}k_{\lambda, \text{black}}\right)\right\} \quad (22)$$

where

$$k_{\lambda} = -0.5 \ln\left\{R_{\lambda, 100\% \text{ coverage}} / R_{\lambda, \text{paper}}\right\} \quad (23)$$

The particular primary and secondary color types are determined using the algorithms listed in Eqs. (9) and (10). Positive areas describe the appropriate color types. Eq. (23) is used to calculate the absorptivity of each color type. Alternatively, one could use the first eigenvector from the single color-type ramp analysis rather than the 100% area coverage sample. This results in a better statistical representation of the colorant. The test target used for this type of analysis is shown in Fig. 15. The resulting first eigenvectors, normalized by their maximum values, are shown in Fig. 16 for the HP650C.

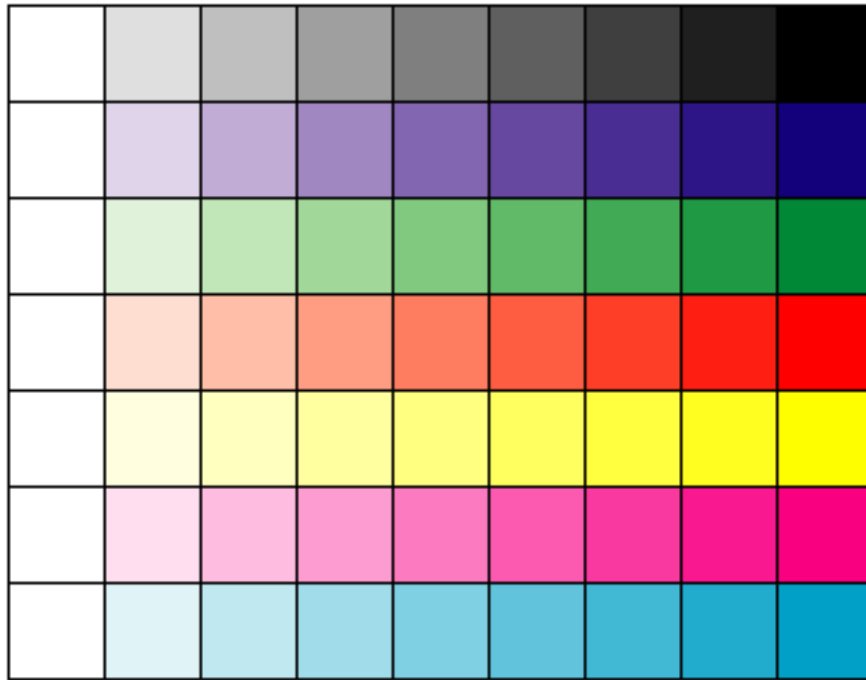


Fig. 15. Test target used to characterize each color type's spectral absorptivity.

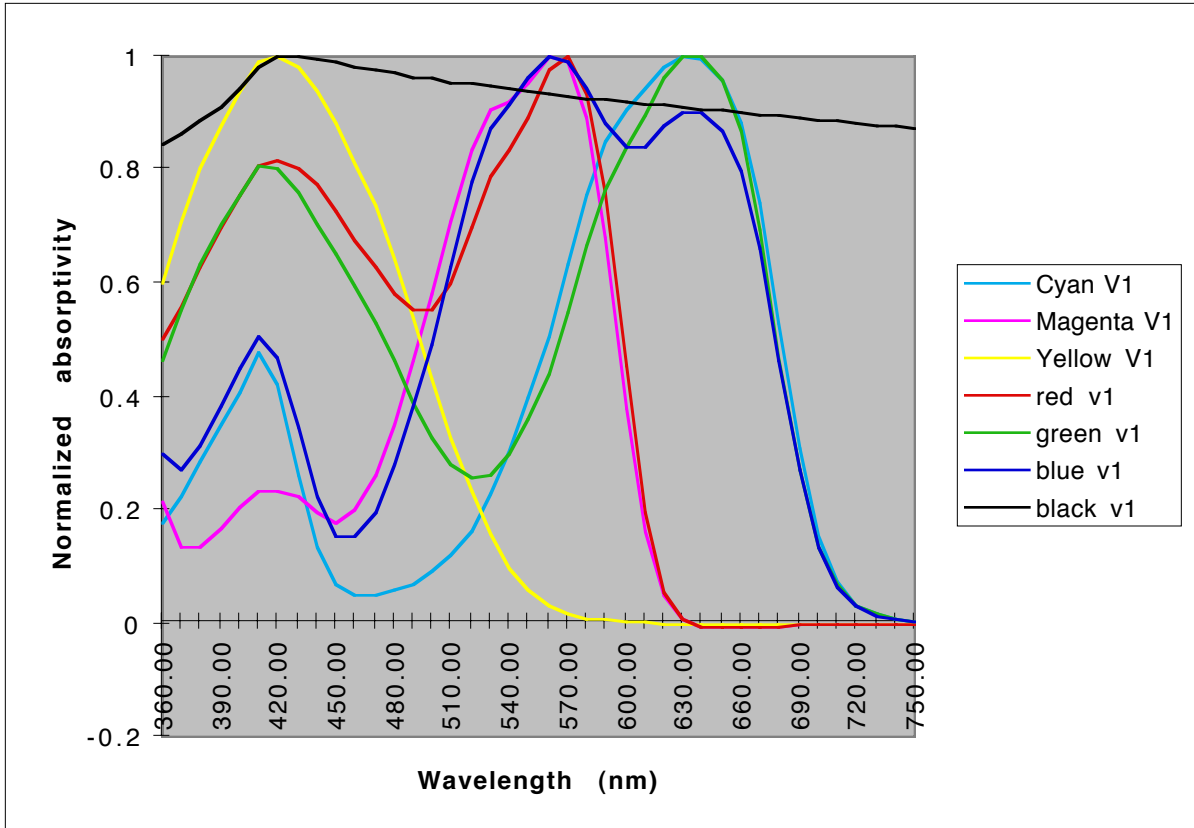


Fig. 16. Normalized absorptivities based on eigenvector analyses of eight possible color types.

Multiple-linear regression is used to estimate the area coverage of each ink:

$$k_{\lambda, \text{measured}} = \beta_{\text{primary}} k_{\lambda, \text{primary}} + \beta_{\text{secondary}} k_{\lambda, \text{secondary}} + \beta_{\text{black}} k_{\lambda, \text{black}} \quad (24)$$

As an example, a sample was printed with 100% magenta, 20% yellow, and 20% black. This corresponds to magenta, red, and black color types. Their spectral absorptivities were used to predict the measured spectral reflectance factor using Eq. (24). The Systat dialog box is shown in Fig. 17. The resulting model fit is given in Fig. 18.

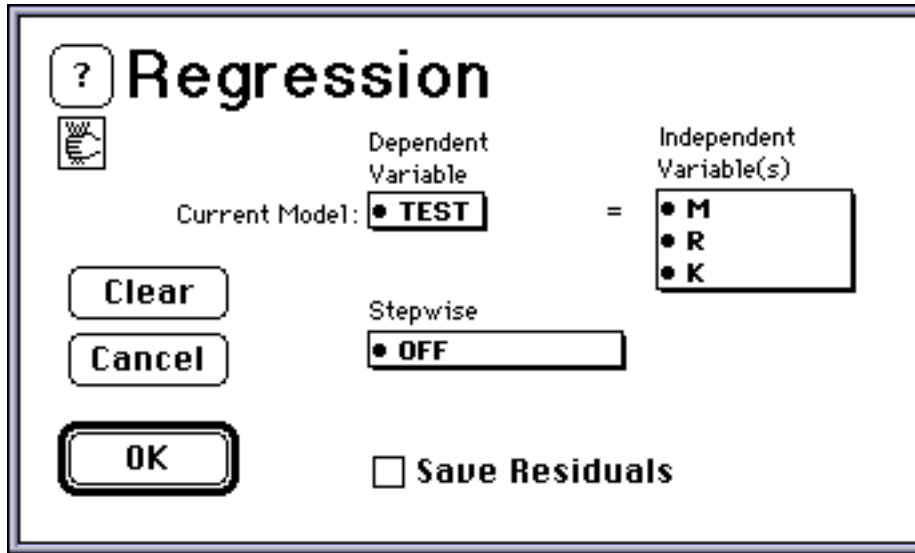


Fig. 17. Systat dialog box for multiple-linear regression.

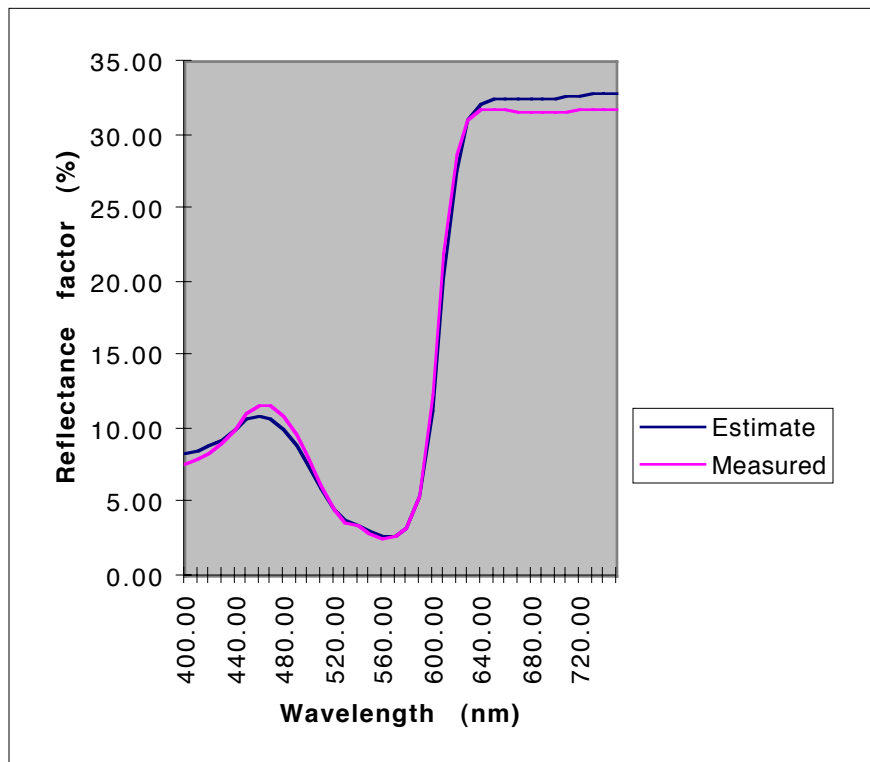


Fig. 18. Modeling result for with 100% magenta, 20% yellow, and 20% black using Eq. 24.

In the event that the color-type selection algorithm shown above is incorrect, a result of proprietary software, one can use stepwise multiple-linear regression and evaluate which color types yield the best result. The Systat dialog box is shown in

Fig. 19 for this procedure. All of the seven color types are considered. For the magenta, red, and black example, the stepwise regression result was identical to that shown in Fig. 18. Thus, for this one color, the algorithm appears to be correct.

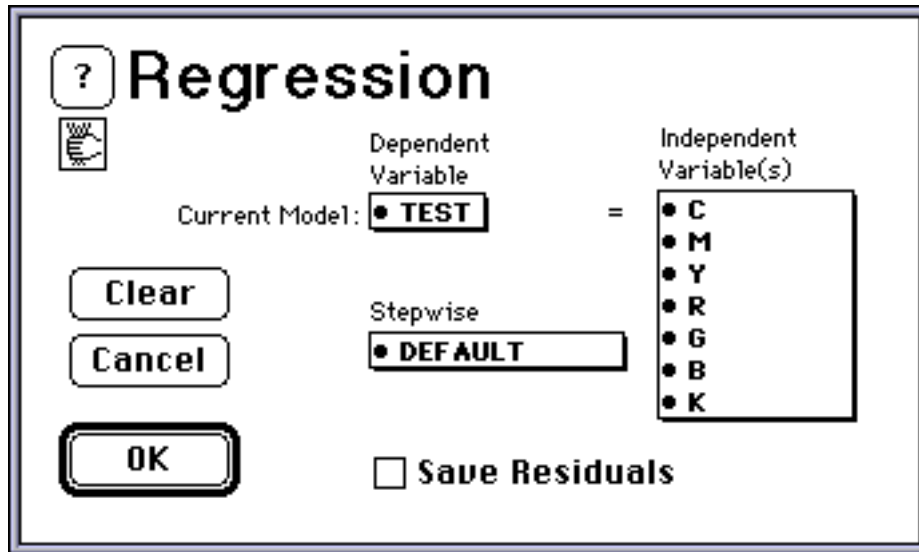


Fig. 19. Systat dialog box for stepwise multiple-linear regression.

In order to complete the forward model, the nonlinear conversion between theoretical dot areas and actual dot areas needs to be determined. This is accomplished by using spectral least squares or colorimetric matching to estimate the effective dot areas for each color of the Fig. 15 target. For example, the concentrations estimated in Table I (spectral least squares) or Table II (colorimetric matching) are plotted against theoretical dot areas calculated using Eqs. (9) and (10). This is shown in Fig. 20. There is a sigmoidal shape to this curve, as opposed to the typical mechanical dot gain function shown in Fig. 4. However, Fig. 20 also includes the data embedded in the one-dimensional printer look-up tables, used to optimize tone reproduction for a given printer. Thus, Fig. 20 represents the product of the printer tone reproduction functions and mechanical dot gain.

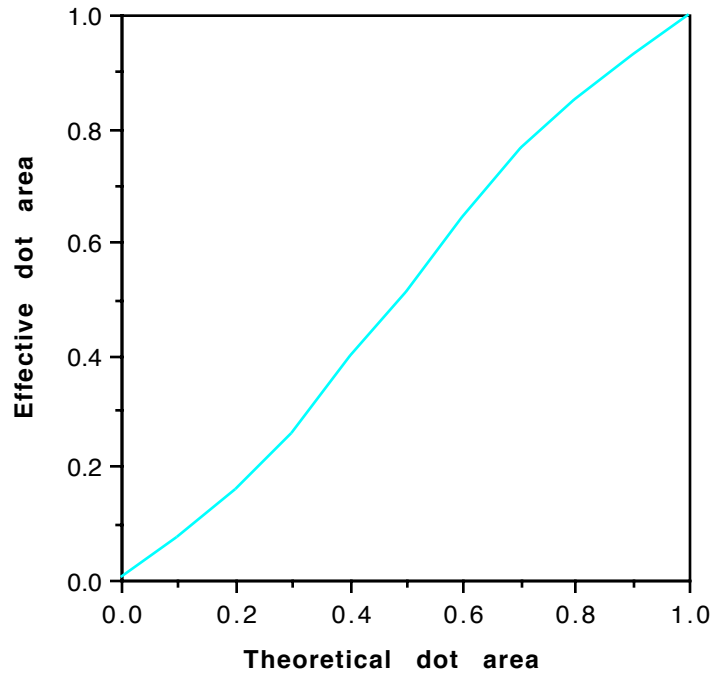


Fig. 20. Mechanical dot gain function for cyan data given in Table I.

A flowchart for model-evaluation is shown in Fig. 21. The first step is to evaluate the halftoning algorithm in order to determine the number of color types. Cluster-dot models correspond to either five color types in the case of four-color printing with 0% GCR (primary, secondary, tertiary, quaternary, paper) or four color types in the case of four-color printing with 100% GCR (primary, secondary, black, paper). Algorithms such as error diffusion often result in sixteen color types for 0% GCR (four color Neugebauer: C, M, Y, C+M, C+Y, Y+M, C+M+Y, K, C+K, M+K,..., C+M+Y+K) or eight color types for 100% GCR. The second step is to hypothesize a color formation model. Examples include Yule-Nielsen-Murray-Davies or Kubelka-Munk. The third step is to evaluate the hypothesized model in its ability to predict primary ramps. The fourth step is to evaluate secondaries and tertiaries. It is important that these ramps are composed of equal amounts of each primary. The primary and secondary ramps are often used to optimize certain model constants (e.g., Yule-Nielsen n value). One should also evaluate color mixtures sampling the color gamut. Spectral or colorimetric matching can be used. The objective is to

determine whether the hypothesized model can reconstruct the measured spectra accurately. In order to build a forward model, the mechanical dot gain of each color type needs to be quantified, the fifth step. To perform this accurately, one needs secondary-ramp samples with equal amounts of constituent primaries. The final step is to evaluate the forward model. It consists of a conversion from digital code values to theoretical dot amounts, the nonlinear step characterizing mechanical dot gain, a nonlinear transformation from spectral reflectance factor to a function of spectral reflectance where linearity is expected, and the linear stage where the color types are linear and additive. One compares the predicted and measured spectra. RMS spectral error and CIELAB ΔE^*_{ab} values are typical goodness metrics.

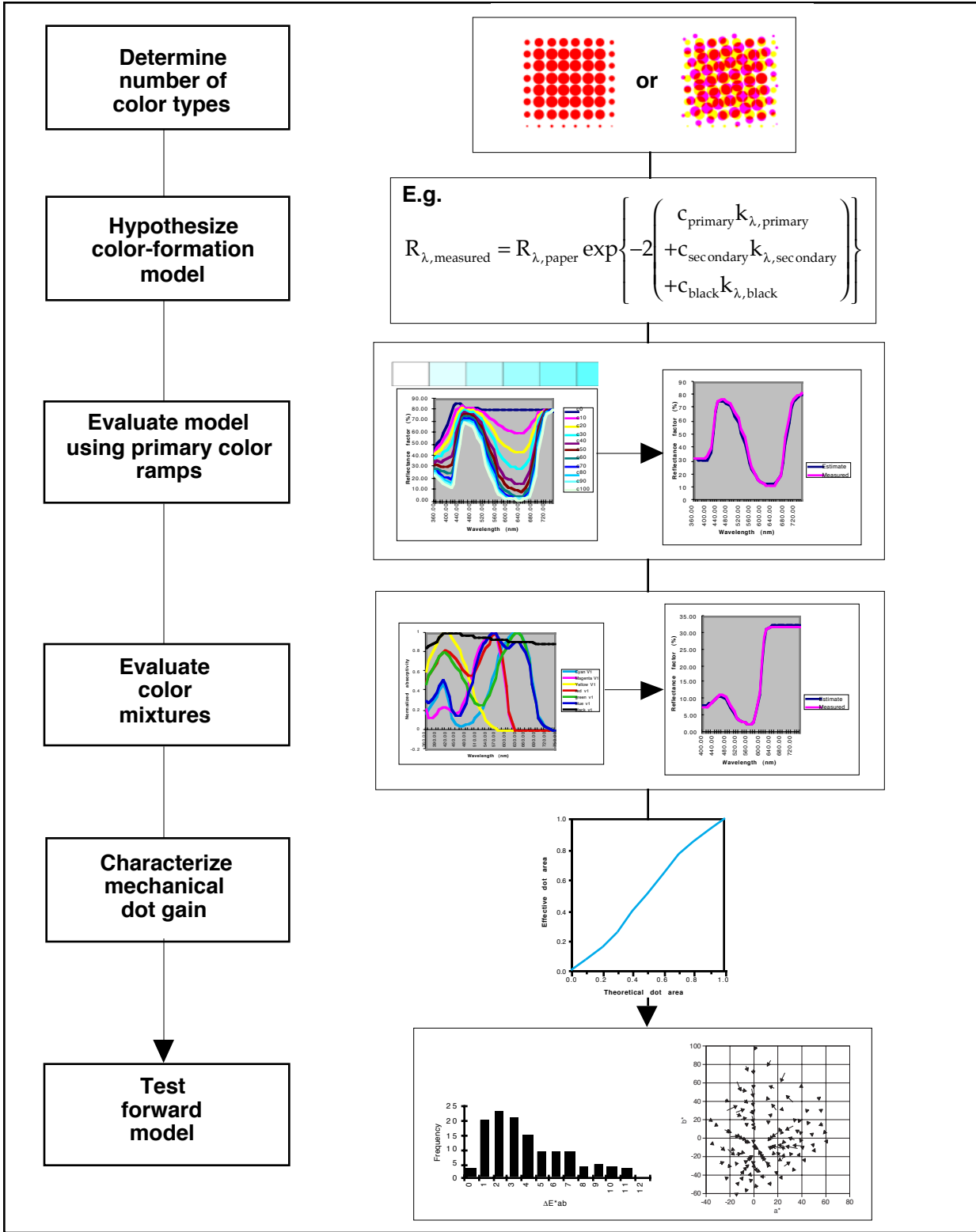


Fig. 21. Model evaluation flowchart.

III. Experimental Example Using HP755CM Large Format Printer

A significant portion of our research evaluating spectral models was performed using the HP650C printer. We encountered severe difficulties in developing a forward model because the conversion from digital code values to the amount of ink delivered to the page was very complex and proprietary. This included secondaries as well as three and four ink mixtures. Near the completion of this project, we received the HP755CM. Our understanding was that the conversion is considerably less complex, although still proprietary. Despite this limitation, one that prevents the development of a model with sufficient accuracy for practical usage, the basic methodology of developing spectral-based models can be demonstrated.

Dataset

Two targets were printed, nine-step ramps of each color type and a 9x9x9 factorial sampling the printer's complete color gamut. The "scatter" halftone algorithm and "best quality" mode options were selected. Uncoated ink-jet paper was used. The ramp target is depicted in Fig. 22.

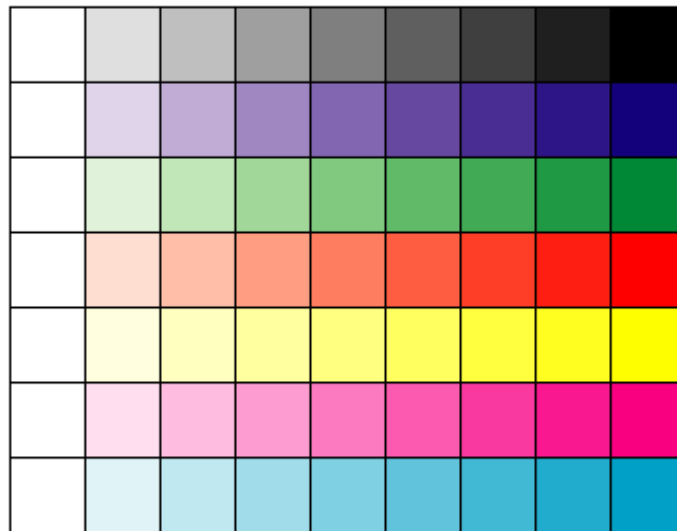


Fig. 22. Ramp target.

The 9x9x9 target consisted of nine pages, and for each page the amounts of cyan and magenta were varied from left to right and top to bottom, respectively. The variation of cyan and magenta ink for each page was in 12.5% increments ranging from 0 to 100%, and they were the same for all nine pages. The amount of yellow ink was fixed for an entire page, and varied from page one through nine at 12.5% increments within the same range as other two inks. The target is shown below in Fig. 23.

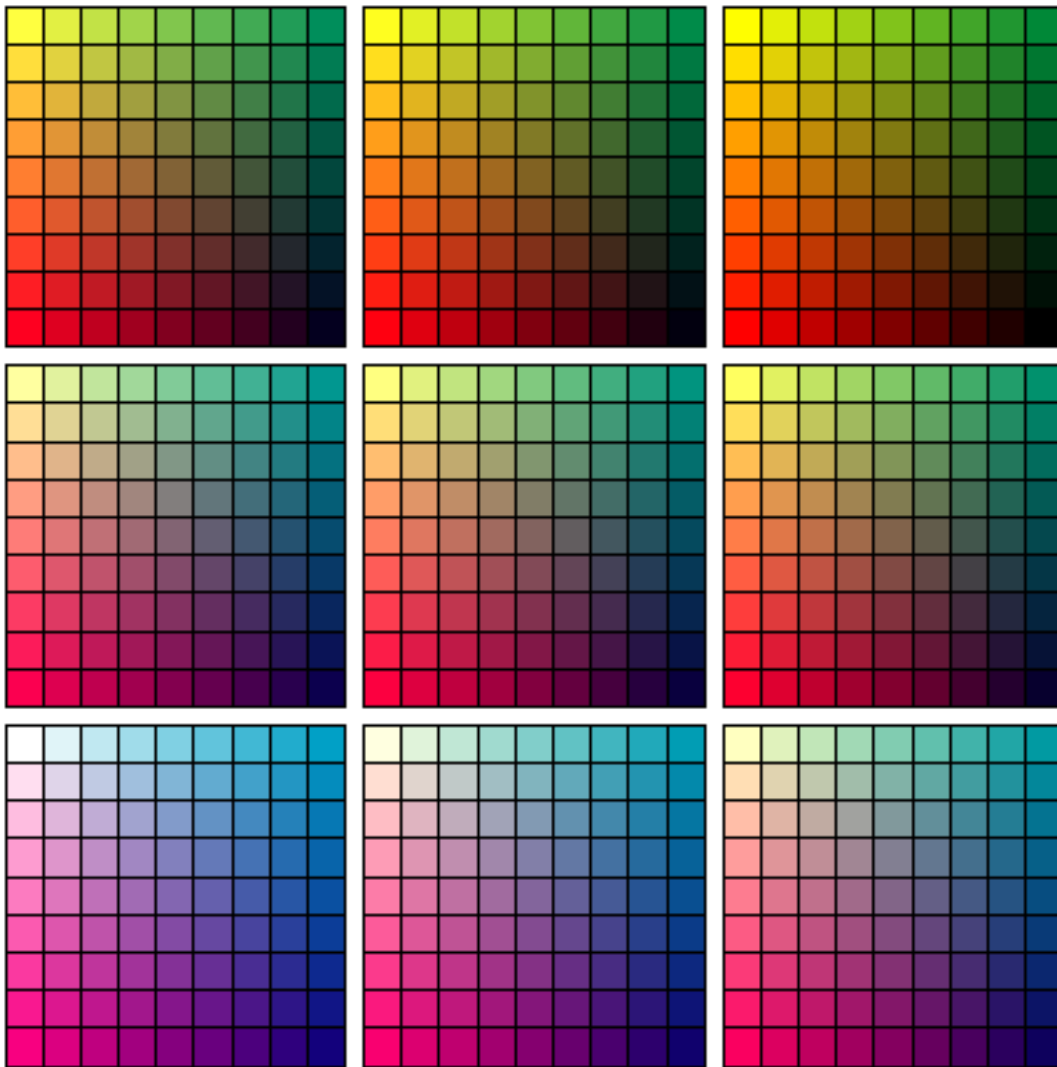


Fig. 23. 9x9x9 verification target.

The spectral reflectance factor of each sample was measured using a Greyttag SPM60 45/0 spectrophotometer. Although our preference was to use an instrument with a larger measurement aperture, the large number of required measurements necessitated an efficient method of measurement and data transfer. A Macintosh-based program provided the required efficiency.

Assumed Halftoning Algorithm

The HP755CM appears to use the identical FM screening algorithm for each color plane. This is shown in Fig. 24 for the blue ramp sample at 25% theoretical area coverage. This halftoning pattern corresponds to cluster-dot printing.

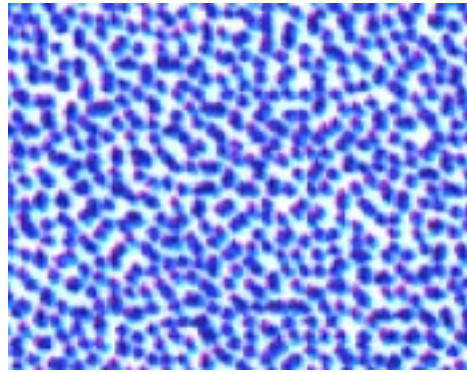


Fig. 24. FM stochastic screening halftoning algorithm of HP755CM (digitized using Sharp JX610 desktop scanner).

The use of the black printer appears to be equivalent to 100% GCR. Thus, the following equations govern the conversion between digital code values and theoretical fractional areas:

$$\begin{aligned}
 d_k &= \min(255 - d_r, 255 - d_g, 255 - d_b) \\
 d_c &= 255 - d_r - d_k \\
 d_m &= 255 - d_g - d_k \\
 d_y &= 255 - d_b - d_k.
 \end{aligned}
 \tag{25}$$

$$\begin{aligned}
a_r &= \min(d_m, d_y) / 255 \\
a_g &= \min(d_c, d_y) / 255 \\
a_b &= \min(d_c, d_m) / 255 \\
a_c &= (d_c / 255) - a_g - a_b \\
a_m &= (d_m / 255) - a_r - a_b \\
a_y &= (d_y / 255) - a_r - a_g \\
a_k &= (d_k / 255) \\
a_w &= 1 - a_r - a_g - a_b - a_c - a_m - a_y - a_k
\end{aligned}
\tag{26}$$

Even if Eqs. (25) and (26) are actual representations of the conversion between digital code values and theoretical fractional areas, there are probably at least one set of additional “rules” that facilitate such things as ink limiting and adjustments to insure particular perceptual attributes of each secondary. In other words, 100% cyan and 100% yellow may not yield a preferred green hue or the paper may become too wet. Ramps of the same ratio of cyan to yellow inks may result in hue shifts. Furthermore, difficulties in dot placement accuracy result in a divergence from the theoretical cluster-dot algorithm. As an illustrative example, the amount of yellow ink in the yellow and green ramps are compared with one another in Fig. 25 for the HP650C where the ink amounts were statistically estimated using spectral matching based on the Kubelka-Munk transparent model. Clearly, Eqs. (25) and (26) would result in large errors when predicting the green ramp.

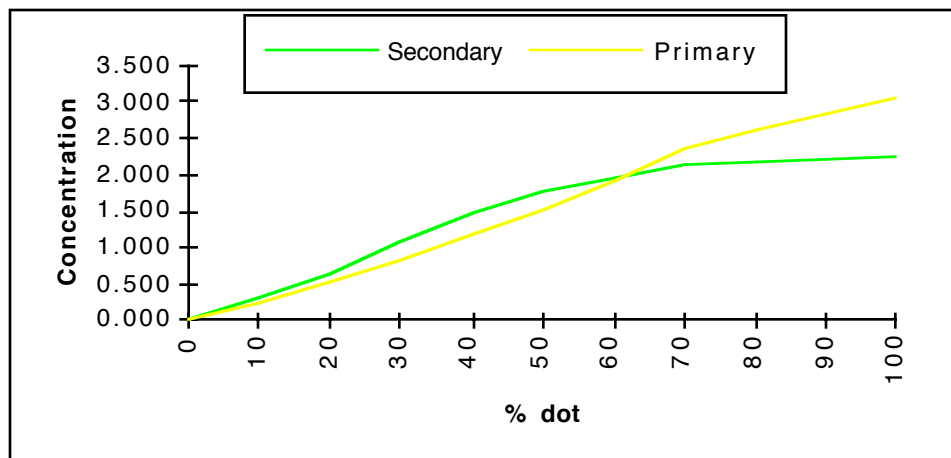


Fig. 25. Concentration of yellow ink in primary and green secondary ramps for HP650C.

The inconsistency in the amount of each primary in secondary ramps is quite evident when viewing printed samples using optical magnification. Figure 26 is a magnification of Fig. 25; it is clear that the blue dots are actually clusters of cyan, magenta, and their blue overlap. From a modeling perspective, it would be very valuable to know whether this is due to additional “rules” governed by one-dimensional LUTs, additional color correction such as error diffusion, or systematic errors in dot placement. In this research, we treated this as either a random error or a systematic effect.

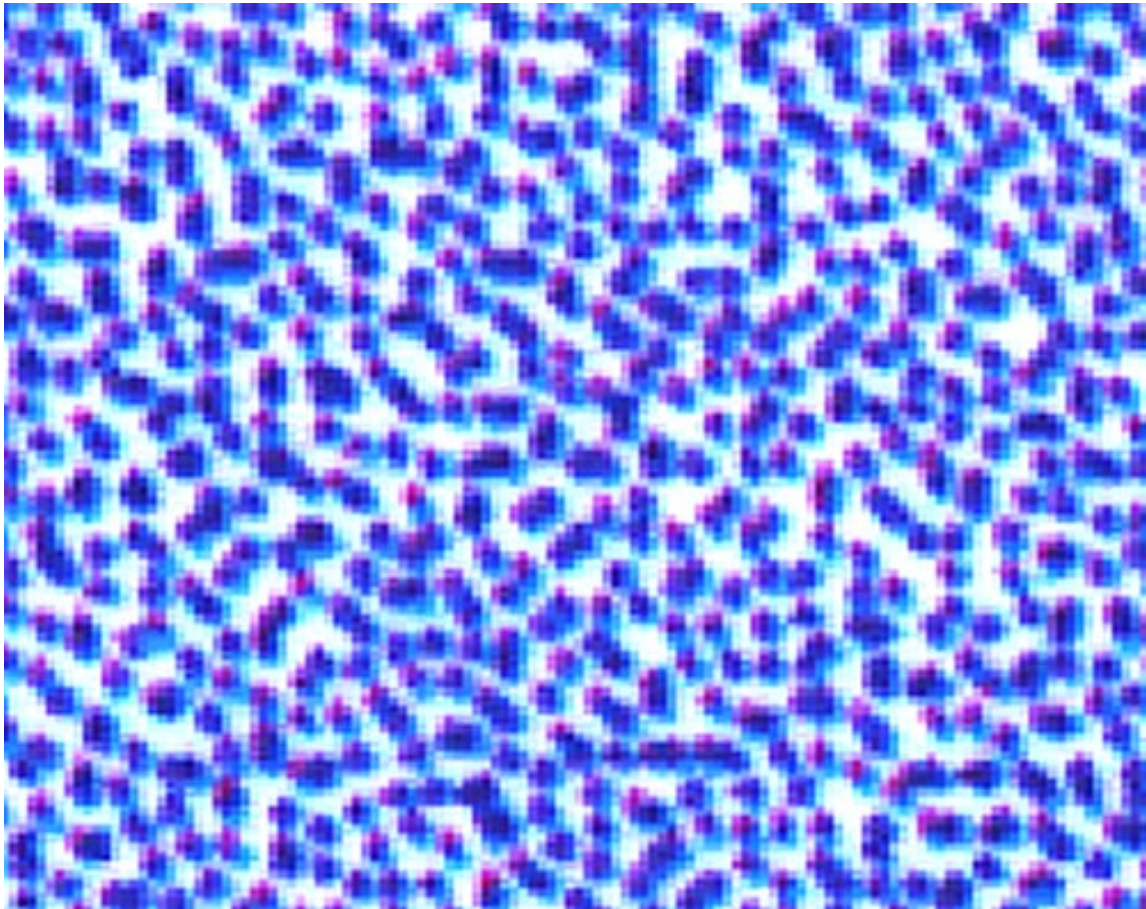


Fig. 26. Magnification of 25% blue ramp sample of HP755CM.

Model Evaluation: Murray-Davies Equation

In theory, ink-jet printing is a halftone process; thus, the Murray-Davies equation should model the spectral reflectance factor measurements of printed images:

$$R_{\lambda} = a_i R_{\lambda,i} + (1 - a_i) R_{\lambda,w} \quad (27)$$

where i represents a particular ramp of interest. Using least squares minimizing spectral error, fractional areas, a , can be estimated. Matlab was used for all the calculations performed on the HP755CM. The results of predicting the primary and secondary ramps are shown below in Fig. 27. CIELAB ΔE^*_{ab} error statistics are shown in Table IV.

Table IV. CIELAB ΔE^*_{ab} error statistics.

Mean	7
Standard Deviation	6.3
Maximum	22.1
Minimum	0

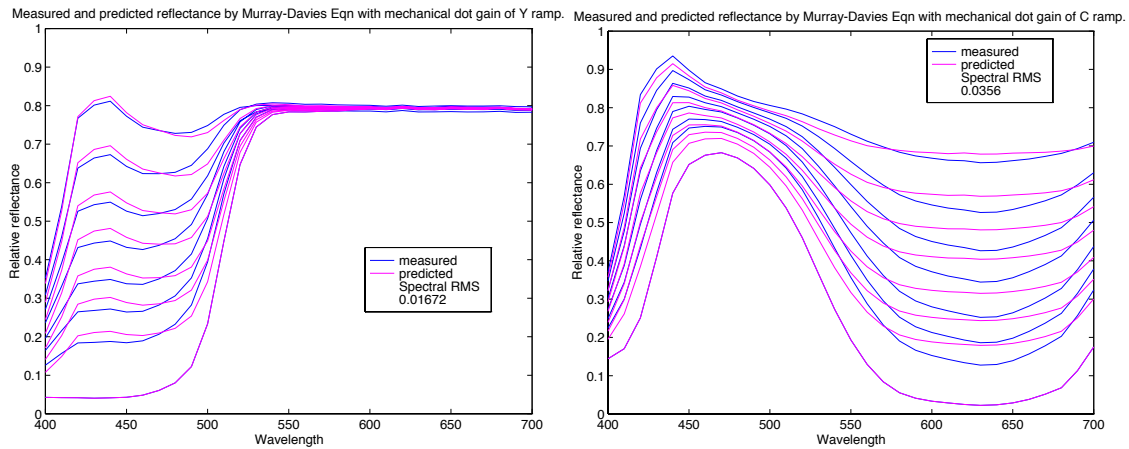


Fig. 27. Primary and secondary ramp predictions using Murray-Davies equation.

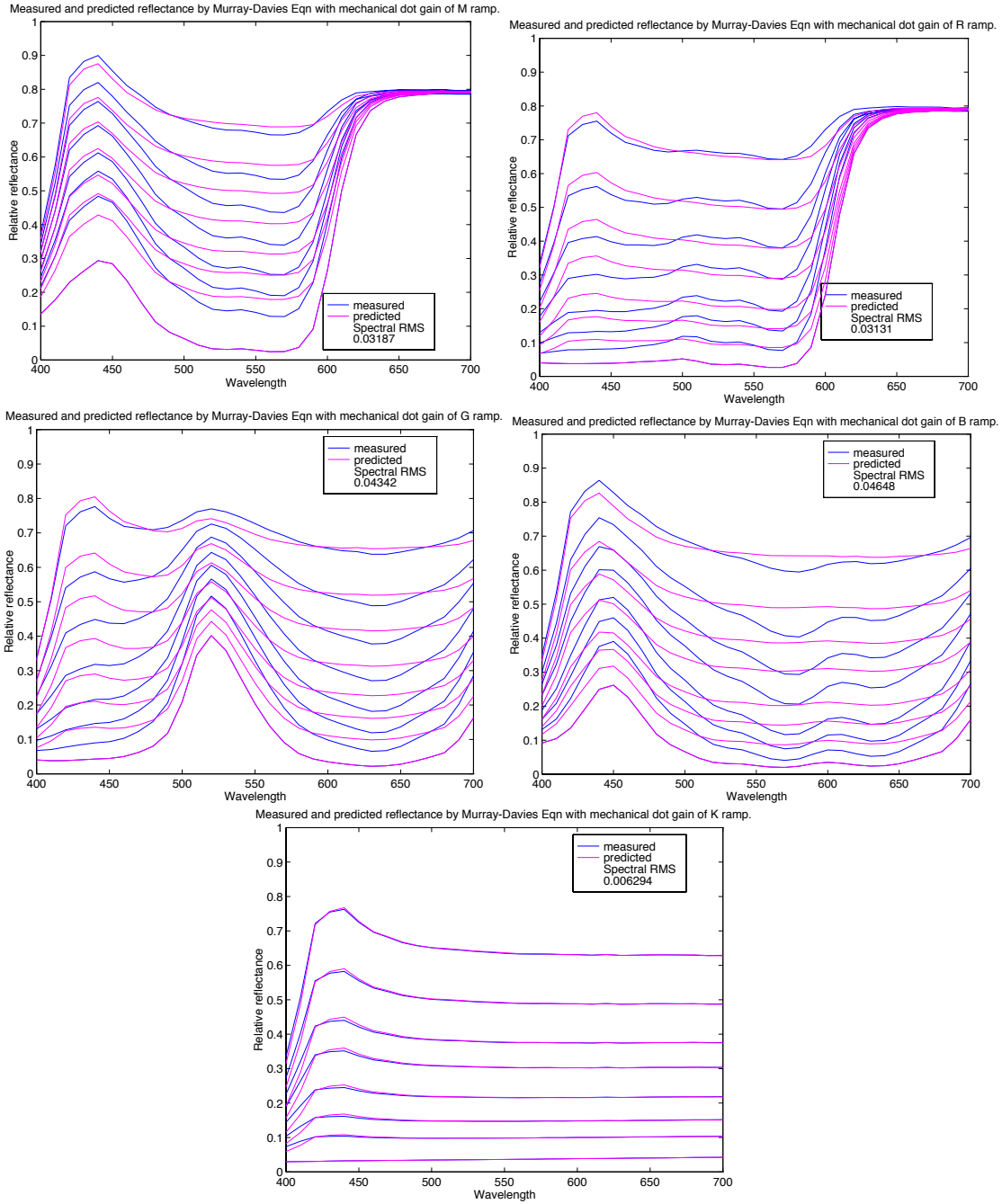


Fig. 27 (cont.). Primary and secondary ramp predictions using Murray-Davies equation.

Figure 27 reveals three important trends. First, absorption bandwidth of the predicted spectra are wider than the measured spectra. This points to optical interactions between the paper and ink, underscoring the need for either the n -value correction or the use of Kubelka-Munk theory. The second trend can be seen

by evaluating the secondary colors. In addition to the bandwidth errors, there are more crossovers between the predicted and measured spectra than between the spectra for the primary ramps. This suggests that there are not equal amounts of each primary used to produce the secondary colors, an anticipated occurrence. Third, the black-ramp colors are very well predicted. This implies that the optical interactions are much less for black ink than chromatic inks. Presumably, the chemistry and surface properties are different between the black and chromatic inks. Also the spectral nonselectivity of black ink simplifies the optical interactions.

The regression results also enable the estimation of mechanical dot gain. Plotting the relationship between the regression coefficients and theoretical dot areas quantifies mechanical dot gain for each primary and secondary. This is shown in Fig. 28. The black dot-gain relationship is typical of photo-mechanical printing where the dot gain is greatest at about 50% area coverage. The secondary colors had greater dot gain than that of the primary colors. This is consistent with increased wetting of the paper resulting in greater ink spread. The shapes of the primary functions are inconsistent with typical printing. Since the abrupt change at 90% theoretical coverage occurred consistently for all three primaries, this is probably a real result and not due to measurement or Postscript encoding errors. There are two possible causes for this. Recall that these functions are a product of mechanical dot gain and tone reproduction via the printer one-dimensional LUTs. These LUTs may be nonlinear in shape. It is possible that with finer sampling than every 10%, the underlying nonlinear shape may be revealed explaining the unexpected behavior. Alternatively, the pipeline between digital data and the actual amount of ink delivered may be complex in order to minimize printing limitations. The unexpected shapes may be indicative of the complex encoding.

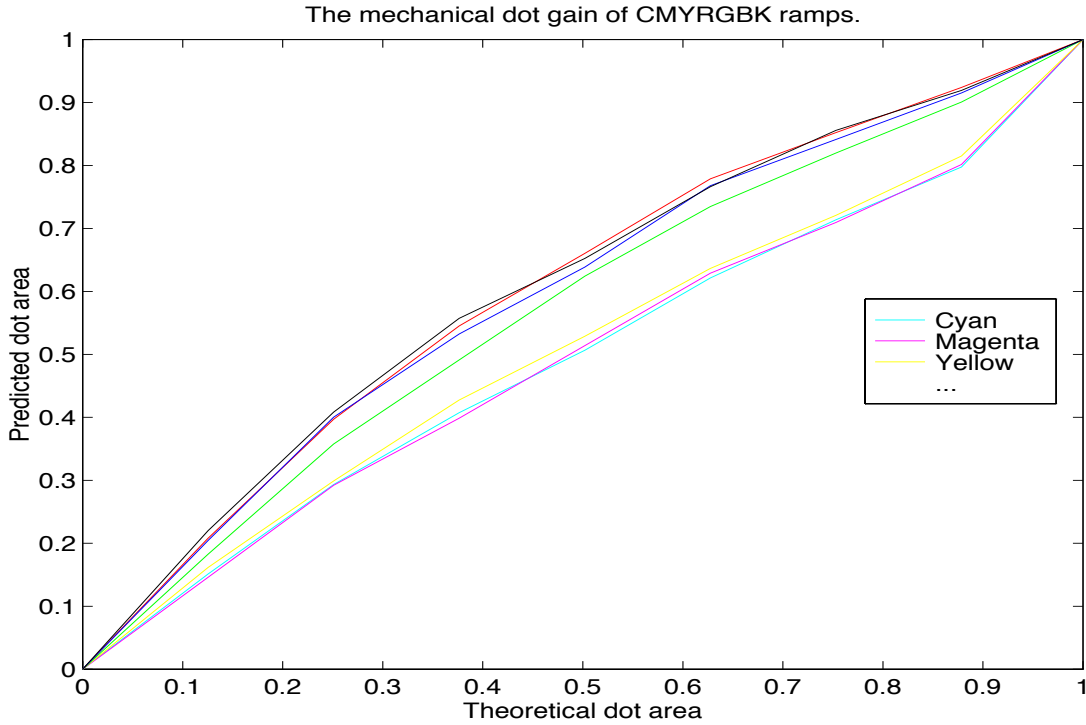


Fig. 28. Mechanical dot gain functions. (Each ramp is appropriately color coded.)

Model Evaluation: Yule-Nielsen-Murray-Davies Equation

The Yule-Nielsen n value can be added to the Murray-Davies equation in order to improve modeling accuracy:

$$R_{\lambda} = \left(a_i R_{\lambda,i}^{1/n} + (1 - a_i) R_{\lambda,w}^{1/n} \right)^n \quad (28)$$

The best way to optimize n is to sweep through various n values, perform the least squares spectral matching, and calculate color differences between the measured and estimated spectra. Plotting average color difference versus n will reveal the optimal n value. This is usually performed using the primary and secondary ramps.

The results of this sweep are shown in Fig. 29. The optimal n value is 6.0. The spectral accuracy for the ramps are shown in Fig. 30. The primaries are reasonably well predicted. However, the secondaries continue to show the unusual crossovers, particularly for the red and blue ramps. This is strong evidence that the secondaries are not composed of equal ratios of each pair of primaries. This has the effect of skewing the n -value optimization. Essentially, n value is used to compensate for spectral errors caused by unequal primary amounts. The color

difference statistics are given in Table V. A histogram is shown in Fig. 31. Small color differences correspond to the primaries. Large color differences are attributed to the secondary colors.

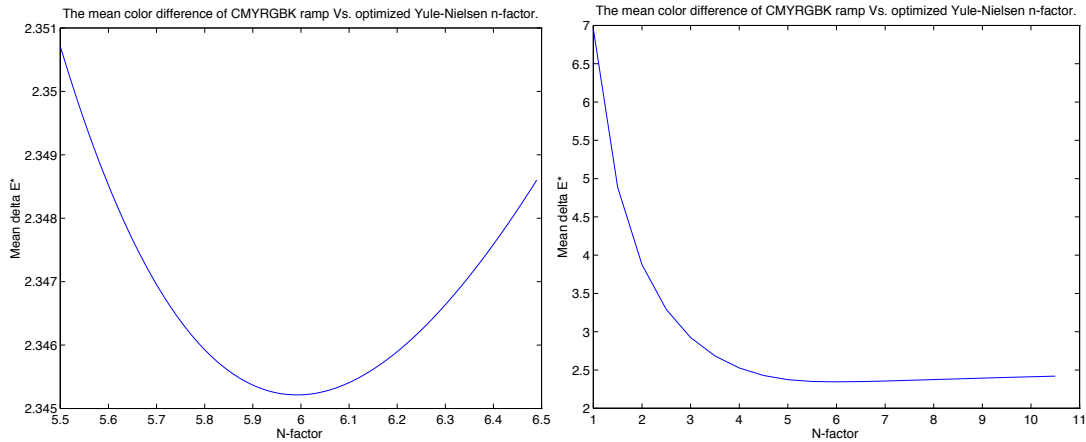


Fig. 29. Optimized Yule-Nielsen n value for CMYRGBK ramps.

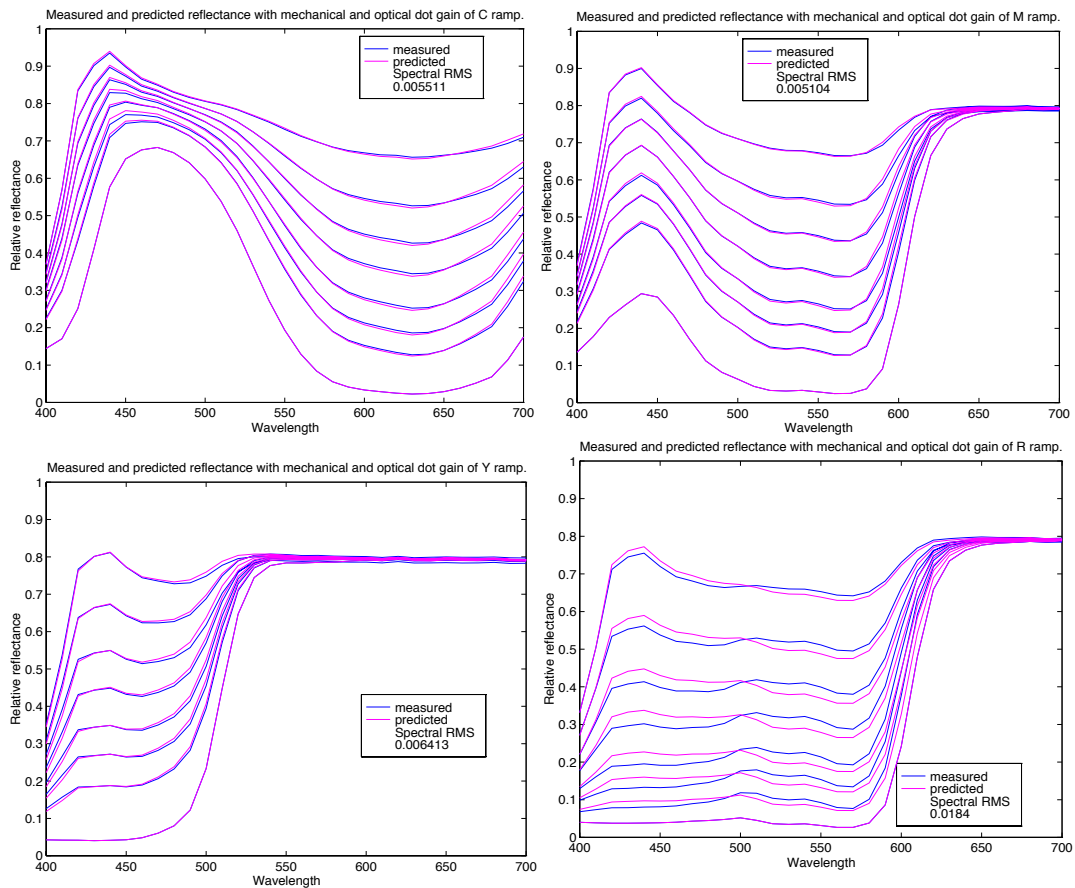


Fig. 30. Primary and secondary ramp predictions using Yule-Nielsen-Murray-Davies equation ($n=6$).

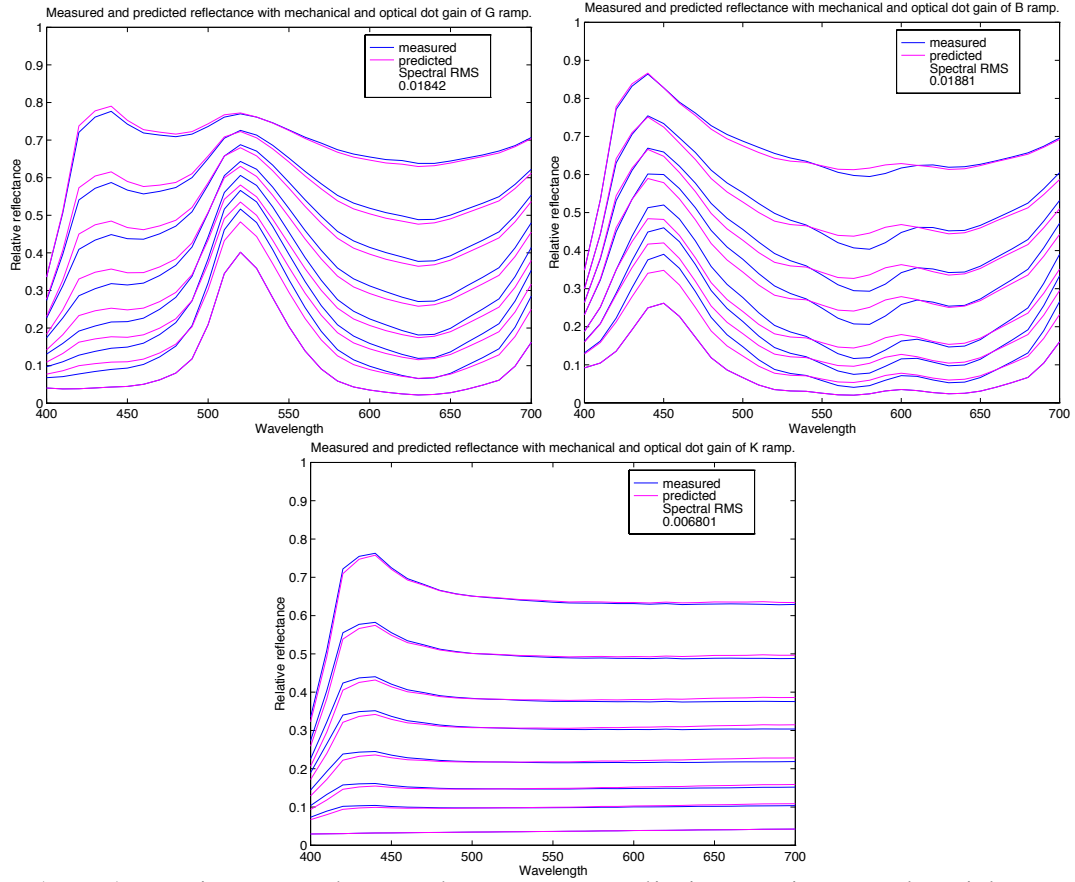


Fig. 30 (cont.). Primary and secondary ramp predictions using Yule-Nielsen-Murray-Davies equation ($n=6$).

Table V. CIELAB ΔE^*_{ab} error statistics using Yule-Nielsen-Murray-Davies equation ($n=6$).

Mean	2.4
Standard Deviation	2.9
Maximum	9.4
Minimum	0

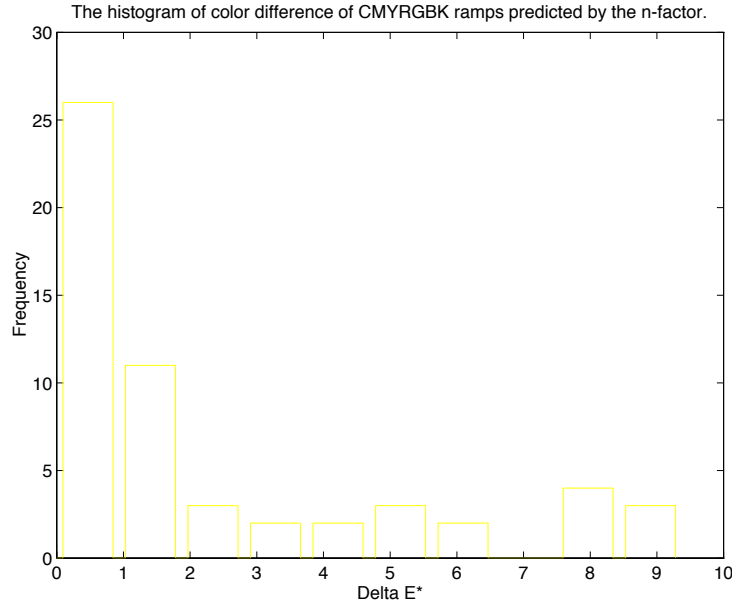


Fig. 31. CIELAB ΔE^*_{ab} histogram for primary and secondary ramp predictions using Yule-Nielsen-Murray-Davies equation.

Because of the skewing of the n value estimation caused by the secondaries, the n -value optimization was repeated using only the primary ramps (C, M, Y, K). This resulted in an optimized n of 5.2, shown in Fig. 32. The spectral reconstruction and colorimetric accuracy statistics for the lower n were nearly identical to those for $n=6.0$. Because n is an exponent, this result was not surprising. However, because this lower n was not confounded by the secondaries, it was used for the remainder of this report.

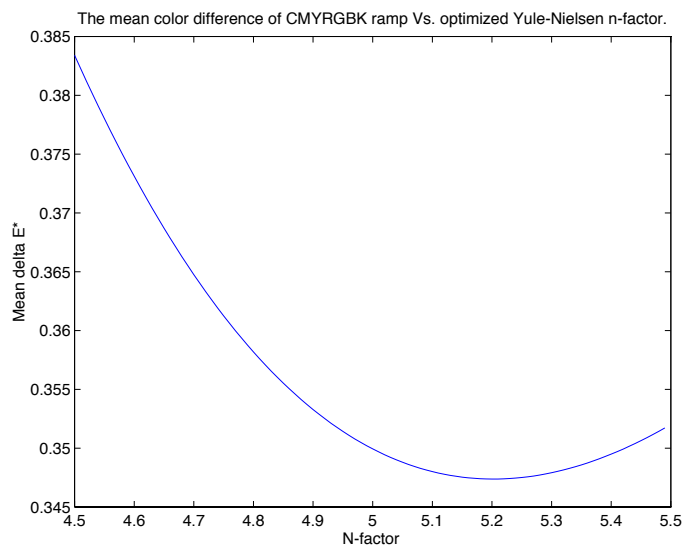


Fig. 32. Optimized Yule-Nielsen n value for CMYK ramps.

The Yule-Nielsen-Murray-Davies equation with $n=5.2$ was used to characterize the mechanical dot gain of each color ramp using least-squares spectral matching. Cubic spline interpolation was used to build seven one-dimensional LUTs, corresponding to each color type. These are plotted in Fig. 33.

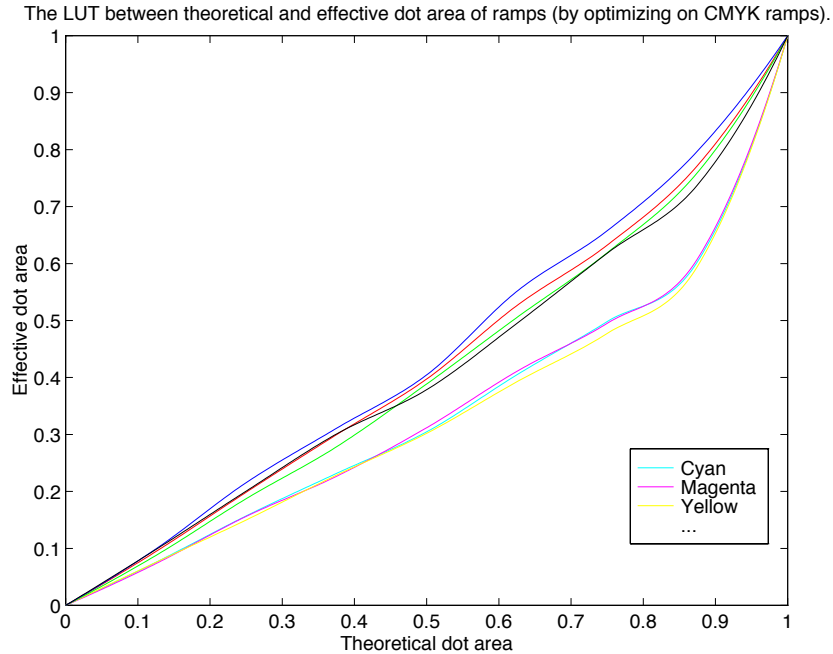


Fig. 33. Mechanical dot gain LUTs for each color type.

The optimal n value (Fig. 32), the mechanical dot-gain functions (Fig. 33), and the color-type selection algorithm [Eqs. (25) and (26)] form the complete forward model. The model accuracy was tested using the 9x9x9 verification target. Large errors are expected since the conversion from digital to dot area is known to be more complex than the theoretical cluster-dot algorithm. The results are given in Table VI. A color-difference histogram is plotted in Fig. 34. The two best and worst predictions, in terms of CIELAB errors, are plotted in Fig. 35.

Table VI. CIELAB ΔE^*_{ab} error statistics for 9x9x9 verification data based on Yule-Nielsen-Murray-Davies model.

Mean	7.4
Standard Deviation	6.5
Maximum	28.0
Minimum	0.2

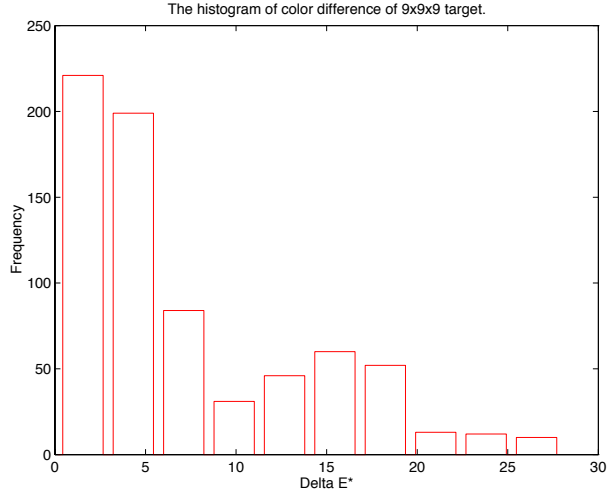


Fig. 34. ΔE^*_{ab} histogram based on Yule-Nielsen-Murray-Davies model.

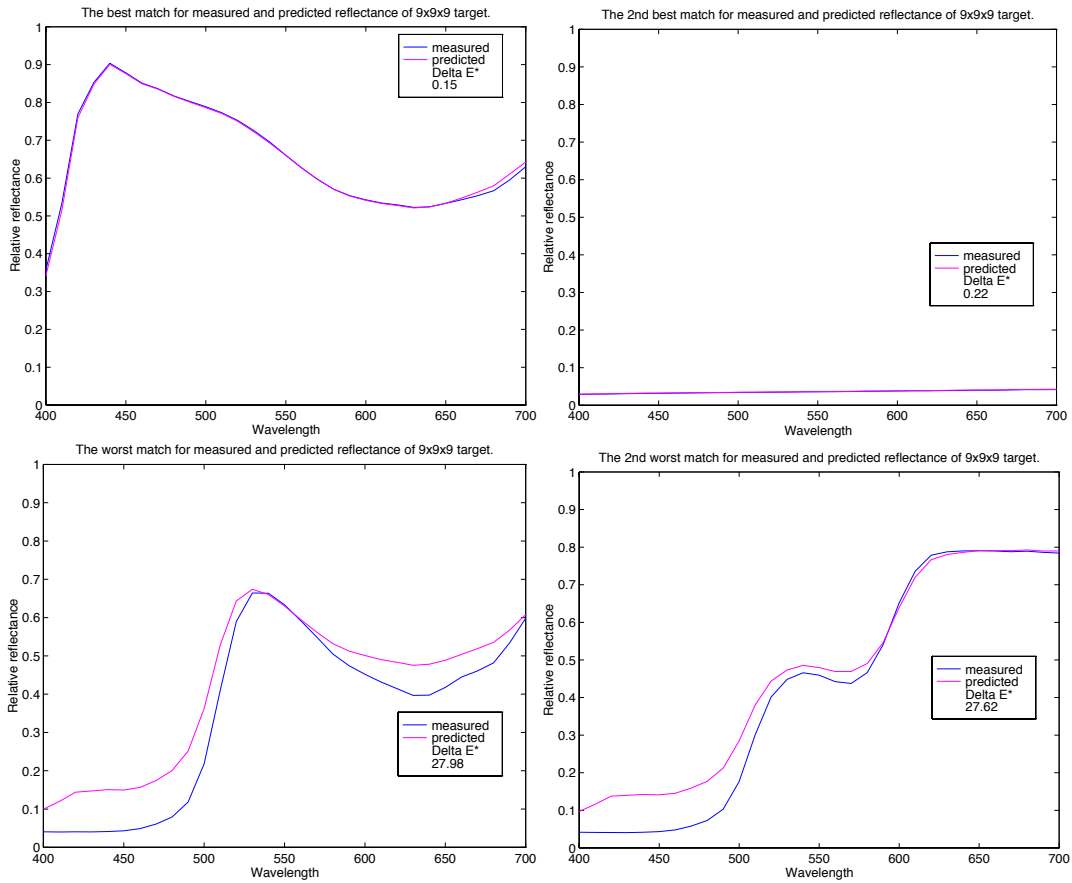


Fig. 35. Two best and two worst predictions of 9x9 verification target based on Yule-Nielsen-Murray-Davies model.

Model Evaluation: Yule-Nielsen-Murray-Davies Equation With Relaxed Colorant Selector

As described in the previous section, the secondaries are not composed of equal amounts of each primary and their dot registrations are not perfect. Despite this knowledge, we assumed these artifacts were random errors. It is possible to relax the cluster-dot color selector algorithm using Eq. 29 where p and s refer to primary and secondary, respectively.

$$\begin{aligned}
 &\text{if } p = c \text{ and } \begin{cases} s = g, \text{ then } p_1 = c \text{ and } p_2 = y \\ s = b, \text{ then } p_1 = c \text{ and } p_2 = m \end{cases} \\
 &\text{if } p = m \text{ and } \begin{cases} s = b, \text{ then } p_1 = m \text{ and } p_2 = c \\ s = r, \text{ then } p_1 = m \text{ and } p_2 = y \end{cases} \\
 &\text{if } p = y \text{ and } \begin{cases} s = g, \text{ then } p_1 = y \text{ and } p_2 = c \\ s = r, \text{ then } p_1 = y \text{ and } p_2 = m \end{cases}
 \end{aligned} \tag{29}$$

Eq. (29) assumes that for a given color, both primaries will be observable, in addition to their overprint and black. This is similar to Neugebauer mixing, but without constraining the dot areas as random probabilities. The color formation equation is given in Eq. (30).

$$R_\lambda = \left(a_{p_1} R_{\lambda, p_1}^{1/n} + a_{p_2} R_{\lambda, p_2}^{1/n} + a_s R_{\lambda, s}^{1/n} + a_k R_{\lambda, k}^{1/n} + (1 - a_{p_1} - a_{p_2} - a_s - a_k) R_{\lambda, w}^{1/n} \right)^n \tag{30}$$

The advantage of this approach is that the limitations encountered with predicting the secondaries are minimized. Using Eq. (30) with n=5.2, the area coverages were estimated for the color ramps using spectral least squares. The resulting dot-gain functions are shown in Fig. 36. The upper-left figure describes the primary ramp relationships. The remaining figures depict the amount of each color type in the red, green, and blue ramps. Notice that the relationships between theoretical areas (essentially a single function for each secondary) and what is estimated statistically are quite different. The lack of registration or the divergence from the theoretical cluster-dot algorithm is evident, supporting the optical evaluations depicted in Fig. 26.

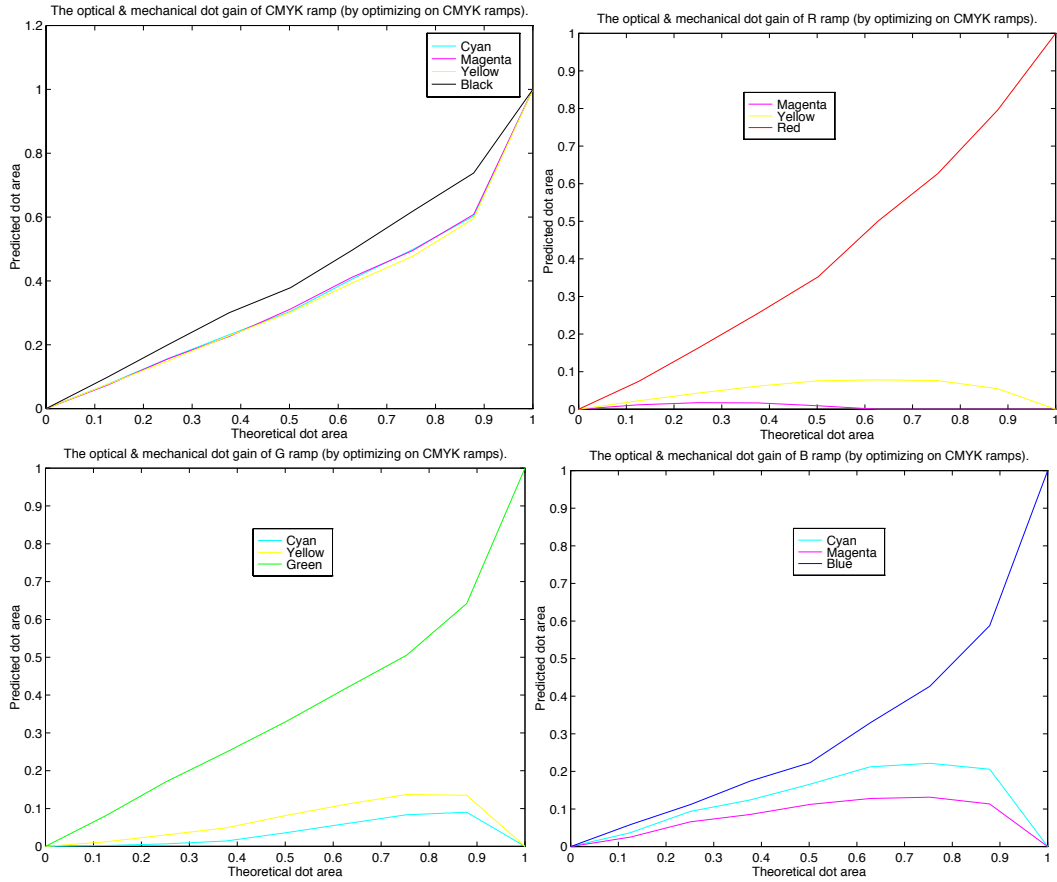


Fig. 36. Mechanical dot gain functions for relaxed-cluster-dot halftone algorithm.

Increasing the number of color types greatly improves the model predictions for the ramp data as shown in Table VII and Fig. 37.

Table VII. CIELAB ΔE^*_{ab} error statistics for ramp data based on Yule-Nielsen-Murray-Davies model with relaxed color-type selector.

Mean	1.2
Standard Deviation	1.4
Maximum	5.9
Minimum	0.2

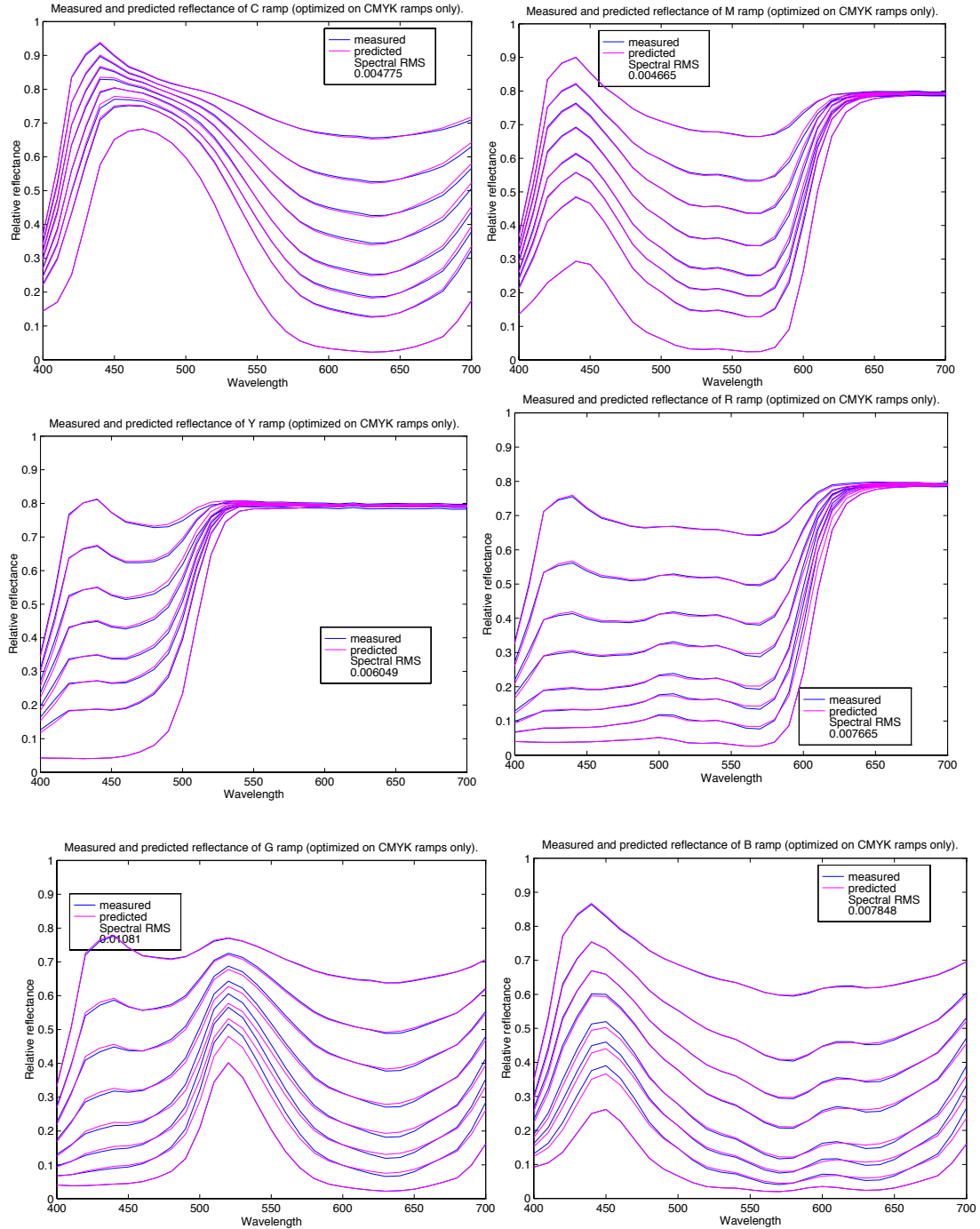


Fig. 37. Primary and secondary ramp predictions using Yule-Niesen-Murray-Davies equation with relaxed color-type selector.

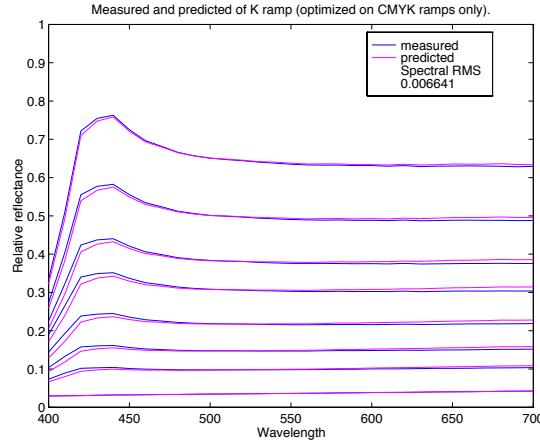


Fig. 37 (cont.). Primary and secondary ramp predictions using Yule-Niesen-Murray-Davies equation with relaxed color-type selector.

The relaxed model was used to predict the 9x9x9 verification target. The colorimetric results are listed in Table VIII. The two best and two worst predictions are plotted in Fig. 38. The results are very similar to the model that does not allow for a second primary. This implies that the relationships based on the secondary ramps do not correlate with colors throughout the color gamut.

Table VIII. CIELAB ΔE^*_{ab} error statistics for 9x9x9 verification data based on Yule-Nielsen-Murray-Davies model with relaxed color-type selector.

Mean	6.4
Standard Deviation	6.6
Maximum	25.9
Minimum	0.1

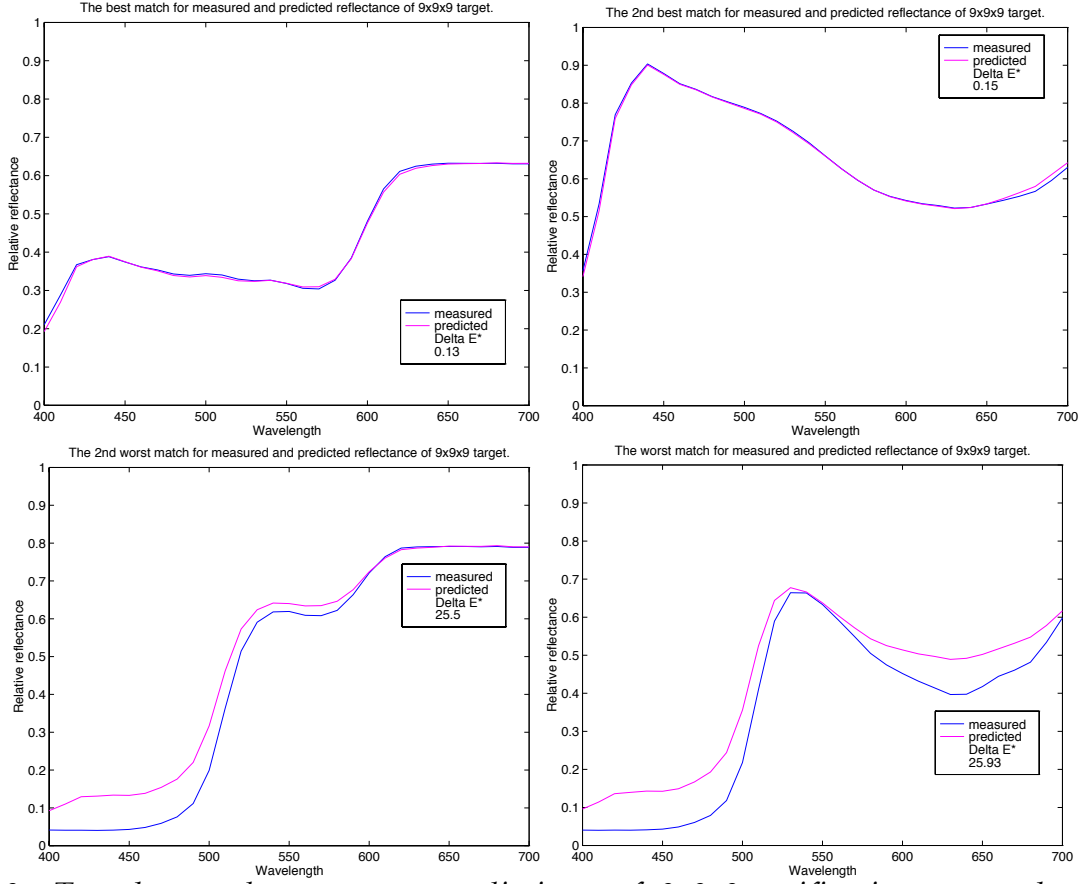


Fig. 38. Two best and two worst predictions of 9x9x9 verification target based on Yule-Nielsen-Murray-Davies model with relaxed color-type selector.

Model Evaluation: Continuous Tone Using Kubelka-Munk Equation

The large n value predicted above suggests that a continuous-tone model may be useful to predict the color formation of the HP755CM. Using the initial cluster-dot algorithm to identify the appropriate primary and secondary, this leads to the appropriate primaries to consider, given by Eq. (31). Colors are predicted using Eq. (32).

$$\begin{aligned}
 \text{if } s = r, & \text{ then } p_1 = m \text{ and } p_2 = y \\
 \text{if } s = g, & \text{ then } p_1 = c \text{ and } p_2 = y \\
 \text{if } s = b, & \text{ then } p_1 = m \text{ and } p_2 = c
 \end{aligned} \quad (31)$$

$$R_{\lambda, \text{measured}} = R_{\lambda, \text{paper}} \exp\left\{-2\left(c_{p_1} k_{\lambda, p_1} + c_{p_2} k_{\lambda, p_2} + c_k k_{\lambda, k}\right)\right\} \quad (32)$$

The mechanical dot gain for the four primary ramps were determined by least squares spectral matching using the absorption spectra where the absorptivities of each primary were based on the 100% area-coverage samples. The dot-gain functions are shown in Fig. 39. The spectral reconstruction accuracy of the primaries are shown in Fig. 40. These reconstructions, although close, are not as accurate as the Yule-Nielsen-Murray-Davies equation with the relaxed color-type selector.

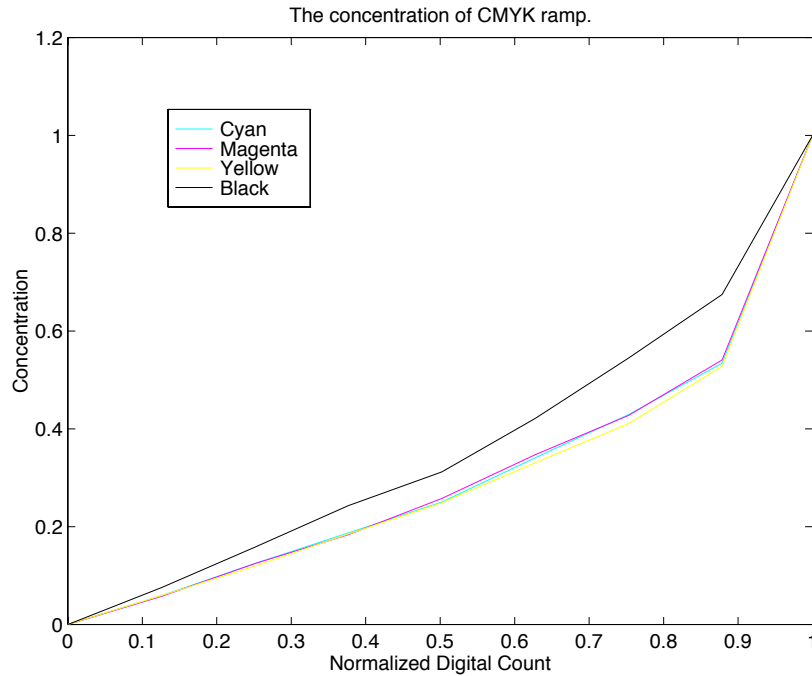


Fig. 39. Mechanical dot gain of CMYK primaries using continuous tone model.

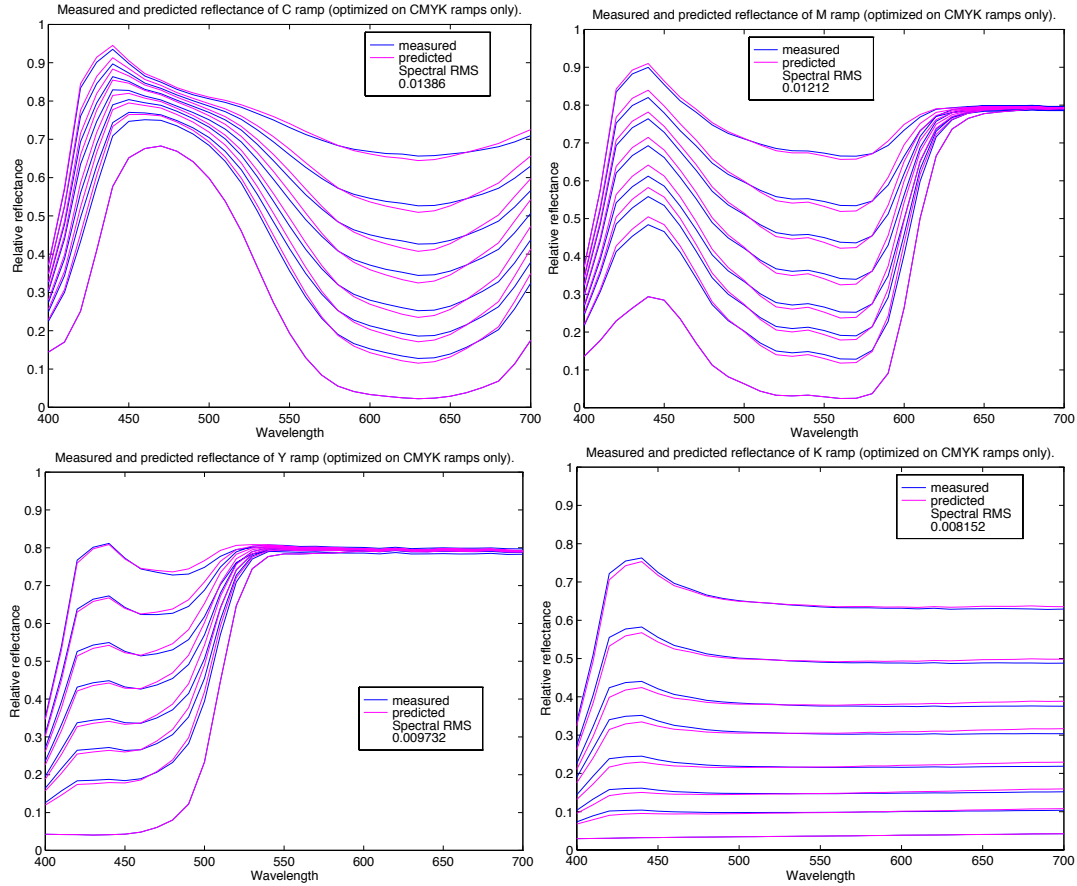


Fig. 40. Primary ramp predictions using continuous tone model with Kubelka-Munk theory.

The continuous-tone model was used to predict the 9x9x9 verification data. The colorimetric performance statistics are shown in Table IX. The two best and worst spectral predictions are plotted in Fig. 41. The results are similar in performance to the Yule-Nielsen-Murray-Davies equation but slightly worse than the Yule-Murray-Davis equation with the relaxed color-type selector.

Table IX. CIELAB ΔE^*_{ab} error statistics for 9x9x9 verification data based on the continuous-tone Kubelka-Munk model.

Mean	7.7
Standard Deviation	6.8
Maximum	28.9
Minimum	0.2

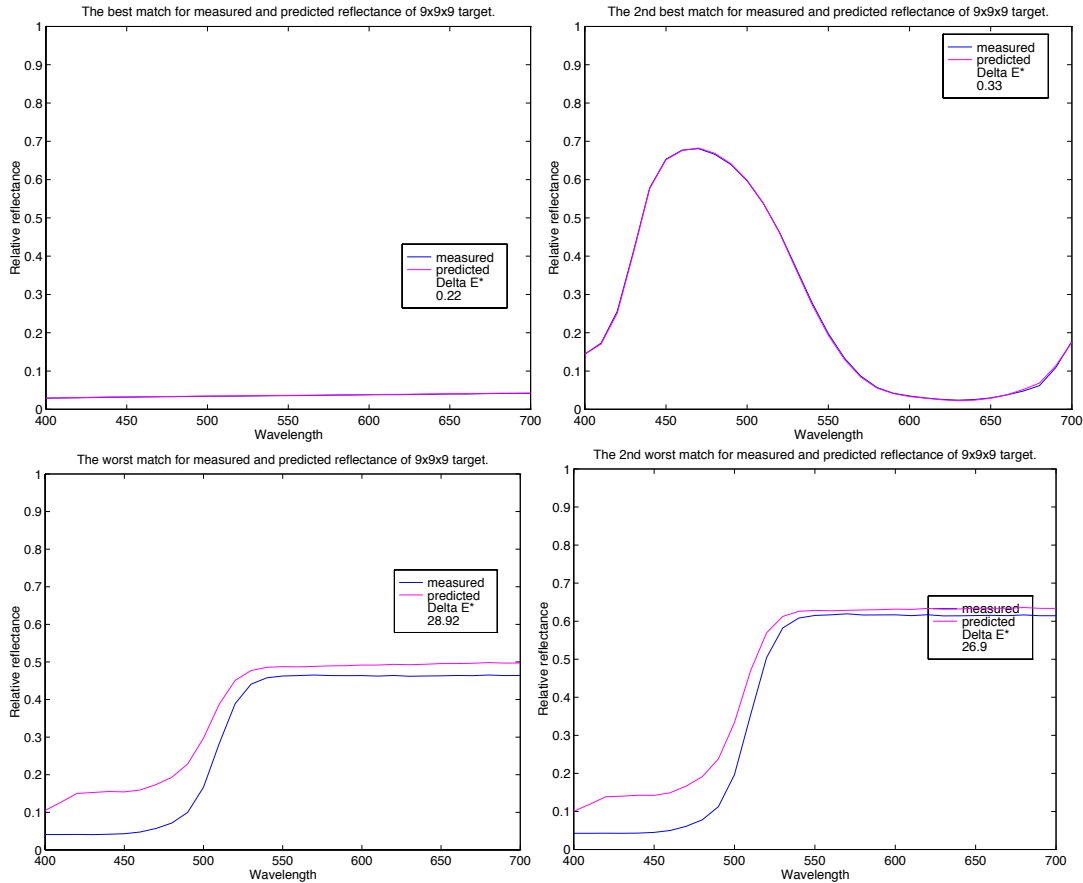


Fig. 41. Two best and two worst predictions of 9x9x9 verification target based on the continuous-tone Kubelka-Munk model.

Selecting the Optimal Model

Three forward models have been developed and tested: the Yule-Nielsen-Murray-Davis equation assuming theoretical cluster-dot ink placement, the Yule-Nielsen-Murray-Davis equation with a relaxed color-type selector, and a continuous-tone equation based on the transparent form of Kubelka-Munk turbid media theory. First, it's worthwhile to evaluate the spectral reconstruction accuracy of the primary ramps. The Spectral RMS errors are summarized in Table X. The Yule-Nielsen-Murray-Davis models were twice as accurate as the continuous-tone Kubelka-Munk model. This is a different result than for the HP650C printer. Presumably, slight differences in ink, substrate, and halftoning caused this difference. However, both models had good performance in predicting the spectral properties of the primary ramps.

The secondaries were much better predicted with the relaxed colorant selector; the RMS errors were half the magnitude compared with the theoretical cluster-dot halftoning algorithm.

Table X. Spectral RMS errors for primary and secondary ramps.

	Yule-Nielsen-Murray-Davis	Yule-Nielsen-Murray-Davis relaxed color-type selector	Continuous tone Kubelka Munk
Cyan	0.0048	0.0048	0.0139
Magenta	0.0047	0.0047	0.0121
Yellow	0.0060	0.0060	0.0097
Black	0.0066	0.0066	0.0082
Red	0.0187	0.0077	
Green	0.0190	0.0108	
Blue	0.0196	0.0078	
CMYK average	0.0055	0.0055	0.0110
RGB average	0.0191	0.0088	

It is prudent to evaluate the verification data, since it was not used to optimize the model parameters. Performance statistics are listed in Table XI. The average performance of the verification data is similar to the results of the primary and secondary ramps. Since the Yule-Nielsen-Murray-Davis model with the relaxed color-type selector has the most degrees of freedom, it is not surprising that it has the best performance. The maximum errors are of the same magnitude. Unfortunately, because the actual digital to dot-area conversion is unknown, these results are inconclusive as shown in Table XI. It is unlikely that these differences are statistically significant given the large standard deviations.

Table XI. Error statistics for 9x9x9 verification data.

	Yule-Nielsen-Murray-Davis	Yule-Nielsen-Murray-Davis relaxed color-type selector	Continuous tone Kubelka Munk
RMS spectral error	0.038	0.038	0.052
Average color difference	7.4	6.4	7.7
Standard deviation color difference	6.5	6.6	6.8
Maximum color difference	28	25.9	28.9
Minimum color difference	0.2	0.1	0.2

We can bypass the actual halftoning pipeline by spectral matching each sample of the verification data set using a particular model. In essence, the dot areas of each color in the verification data are estimated that minimize RMS spectral error. This bypasses the digital to dot-area conversion process. The model that results in the smaller error statistics would indicate the preferred model. The Yule-Nielsen-Murray-Davis model with the relaxed color-type selector and the continuous tone models were evaluated. One potential problem with spectral matching is constraining the dot areas (or concentrations for the continuous tone model) to range between zero and unity. A constrained optimization was implemented to avoid this potential problem. The results are summarized in Table XII. Color-difference histograms are shown in Figs. 42 and 43.

Table XII. Error statistics for 9x9x9 verification data using constrained spectral matching.

	Yule-Nielsen-Murray-Davis relaxed color-type selector	Continuous tone Kubelka Munk
RMS spectral error	0.0068	0.0095
Average color difference	1.2	1.7
Standard deviation color difference	1.3	1.3
Maximum color difference	11.8	6.6
Minimum color difference	0.0	0.1

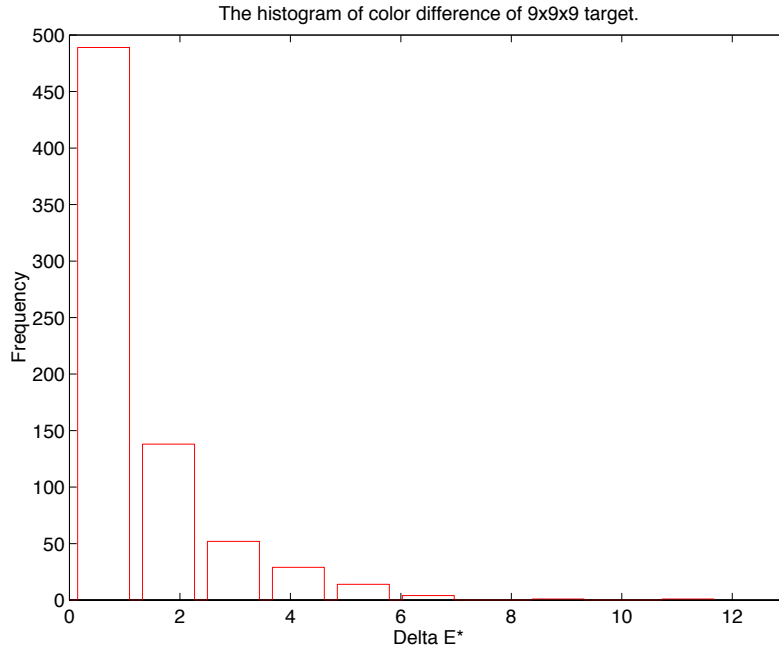


Fig. 42. CIELAB color difference histogram for Yule-Nielsen-Murray-Davis relaxed color-type selector model.

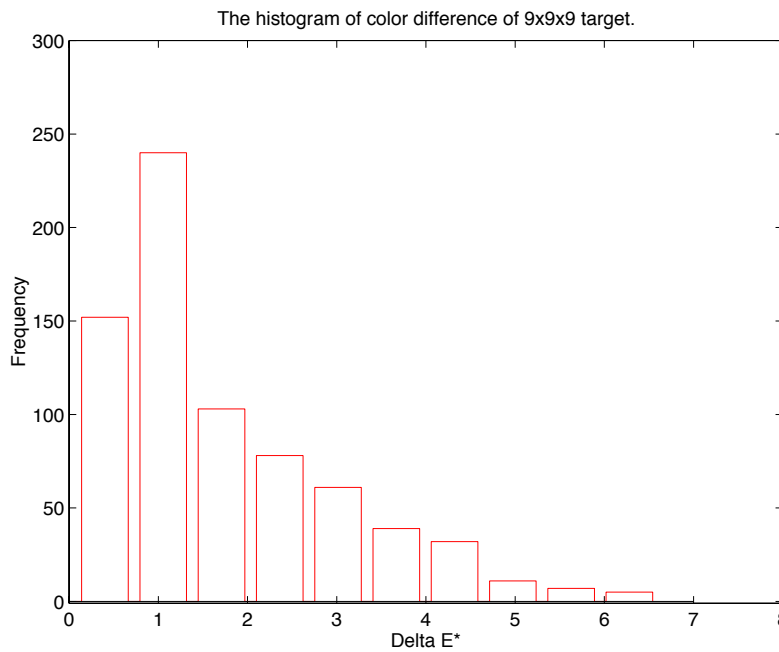


Fig. 43. CIELAB color difference histogram Continuous tone Kubelka Munk model.

The results clearly indicate that the Yule-Nielsen-Murray-Davis model with the relaxed color-type selector is the more appropriate model for describing the spectral properties of the HP 755CM printer. The majority of samples are very well predicted. The four worst samples are plotted in Fig. 44. The samples with color

differences above 7.0 are probably outliers. It appears that the wrong colorants were selected to optimize. This could be caused by measuring the wrong sample (recall that the 729 samples were measured by hand) or a measurement placement error (which would be equivalent to measuring the wrong sample). It is also possible that the constrained optimization converged on a local rather than true minimum value for these two samples. The two green samples with color differences in the $6 \Delta E^*_{ab}$ range appear to be true model limitations.

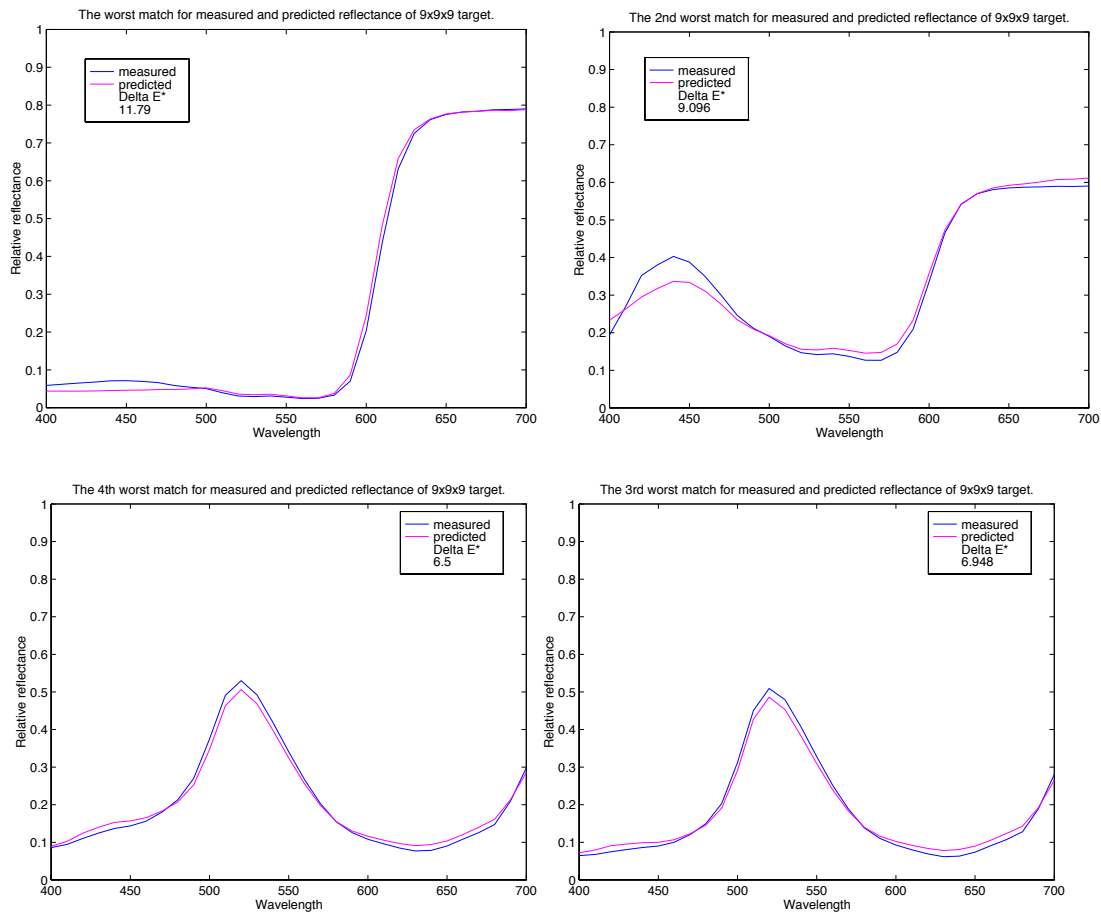


Fig. 44. Four worst predictions for the Yule-Nielsen-Murray-Davis relaxed color-type selector model based on constrained spectral matching.

IV. Summary and Conclusions

Three spectral models were evaluated in terms of their spectral reconstruction accuracy for color images generated using the “scatter mode” on a HP755CM large-format printer. The first model was the Yule-Nielsen-Murray-Davies equation with a cluster-dot halftone algorithm and 100% gray-component replacement. The optimal n value was found to be 5.2. Although this model well predicted primary halftone tints, secondaries and tertiaries were poorly predicted. This was due to limitations in the cluster-dot algorithm in correlating with the actual printed color types. Because of either dot-placement limitations or proprietary HP halftoning algorithms, both primaries were always observable. This led to a relaxed-color-type selector, similar in concept to the Neugebauer equations, but without constraining the dot areas to conform to random variables. This enhancement well predicted all mixtures. The third model was a continuous tone model, where the transparent form of Kubelka-Munk turbid media theory was used to predict printed colors. The modeling results were intermediate to the two halftone models.

For this technology, the Yule-Nielsen-Murray-Davies equation with a relaxed-cluster-dot halftone algorithm is the optimal model to predict spectral reflectance factor of printed images. This can be combined with the digital to dot-area conversion to build device profiles for color management.

V. General References

- E. Allen, "Colorant formulation and shading," in F. Grum and C.J. Bartleson, Eds., *Optical Radiation Measurements Volume 2 Color Measurement*, Academic Press, New York, 1980.
- R. Balasubramanian, "A printer model for dot-on-dot halftone screens," *Proc. SPIE/IS&T Color Imaging Conference: Color Hardcopy*, (1995).
- R. S. Berns, "Methods for characterizing CRT displays", *Displays*, **16**, 173-182 (1996).
- R. S. Berns, "Spectral modeling of a dye diffusion thermal transfer printer," *J. Electronic Imaging*, **2**(4), 359-369 (1993).
- R. S. Berns, R. J. Motta, and M. E. Gorzynski, "CRT colorimetry, part I: theory and practice" *Color Res. Appl.* **18**, 299-314 (1993).
- P. G. Engeldrum, "Four color reproduction theory for dot formed imaging systems," *J. Imaging Technology*, **12**, 126-130 (1986).
- H. R. Kang, "Kubelka-Munk modeling of ink jet ink mixing," *J. Imaging Tech.* **17**, 76-83 (1991).
- H. R. Kang, "Comparison of color mixing theories for use in electronic printing," *IS&T/SID's Color Imaging Conf.: Transforms & Transportability of Color*, 78-82 (1993).
- H. R. Kang, "Applications of color mixing models to electronic printing," *J. Electronic Imaging*, **3**(3), 276-287 (1994).
- P. Kubelka, "New contributions to the optics of intensely light-scattering materials. Part I," *J. Opt. Soc. Am.* **38**, 448-457, 1067 (1948).
- Y. Liu, "Spectral reflectance modification of Neugebauer equations," *Proc. 1991 of Technical Assoc. Graphics Arts*, 154-172 (1992).
- A. Murray, "Monochrome Reproduction in Photoengraving," *J. Franklin Inst.*, **221**, 721-744 (1936).

- H. E. J. Neugebauer, "Die theoretischen grundlagen des mahrfarbenbuchdrucks," *Zeitschrift fur Wissenschaftliche Photographie Photophysik und Photochemie* **36:4**, 73-89 (1937).
- International Color Consortium Profile Format, Version 3.2, anonymous FTP: <ftp://sgigate.sgi.com/pub/icc/ICC32.pdf> (1995).
- N. Ohta, "Estimating absorption bands of component dyes by means of principal component analysis," *Anal. Chem.* **45**, 553-557 (1973).
- R. H. Park and E. I. Stearns, "Spectrophotometric formulation," *J. Opt. Soc. Am.* **34** 112-113 (1944).
- K. H. Parton and R. S. Berns, "Color modeling ink-jet ink on paper using Kubelka-Munk theory," *Proceedings Seventh International Congress on Advances in Non-Impact Printing Technologies*, 271-280 (1992).
- M. Pearson, "n-value for general conditions," *Proc. 1980 of Technical Assoc. Graphics Arts*, 415-425 (1980).
- I. Pobboravsky and M. Pearson, "Computation of dot areas required to match a colorimetrically specified color using the modified Neugebauer equations," *Proc. 1972 of Technical Assoc. Graphics Arts*, 917-927 (1972).
- R. Rolleston and R. Balasubramanian, "Accuracy of various types of Neugebauer model," *Proc. IS&T and SID's Color Imaging Conference: Transforms & Transportability of Color*, 32-37 (1993).
- Y. Shiraiwa and T. Mizuno, "Equation to predict color of halftone prints considering the optical property of paper," *J. Imaging Sci. Tech.* **37**, 385-391 (1993).
- J. A. C. Yule and W. J. Nielsen, "The penetration of light into paper and its effect on halftone reproduction," *Proc. 1951 of Technical Assoc. Graphics Arts*, 65-76 (1951).
- J. A. S. Viggiano, "The color of halftone tints," *Proc. 1985 of Technical Assoc. Graphics Arts*, 647-661 (1985).

J. A. S. Viggiano, "Modeling the color of multi-colored halftones," *Proc. 1990 of Technical Assoc. Graphics Arts*, 44-62 (1990).